batteries

MDPI

Article

The Long-Term Usage of an Off-Grid Photovoltaic System with a Lithium-Ion Battery-Based Energy Storage System on High Mountains: A Case Study in Paiyun Lodge on Mt. Jade in Taiwan

Hsien-Ching Chung

Department of Research and Design, Super Double Power Technology Co., Ltd., Changhua City 500042, Taiwan; hsienching.chung@gmail.com

Abstract: Energy supply on high mountains remains an open issue since grid connection is not feasible. In the past, diesel generators with lead–acid battery energy storage systems (ESSs) were applied in most cases. Recently, photovoltaic (PV) systems with lithium-ion (Li-ion) battery ESSs have become suitable for solving this problem in a greener way. In 2016, an off-grid PV system with a Li-ion battery ESS was installed in Paiyun Lodge on Mt. Jade (the highest lodge in Taiwan). After operating for more than 7 years, the aging of the whole electric power system became a critical issue for its long-term usage. In this work, a method is established for analyzing the massive energy data (over 7 million rows), such as daily operation patterns, as well as the C-rate, temperature, and accumulated energy distributions, and estimating the health of the Li-ion battery system. A completed electric power improvement project dealing with power system aging is reported. Based on the long-term usage experience, a simple cost analysis model comparing lead–acid and Li-ion battery systems is built, revealing that expensive Li-ion batteries can compete with cheap lead–acid batteries for long-term usage on high mountains. This case study can provide engineers and researchers with a fundamental understanding of the long-term usage of off-grid PV ESSs and engineering on high mountains.

Keywords: lithium-ion battery; power improvement; high mountain; cost analysis; Paiyun Lodge

check for updates

Citation: Chung, H.-C. The Long-Term Usage of an Off-Grid Photovoltaic System with a Lithium-Ion Battery-Based Energy Storage System on High Mountains: A Case Study in Paiyun Lodge on Mt. Jade in Taiwan. *Batteries* **2024**, *10*, 202. https://doi.org/10.3390/batteries10060202

Academic Editor: Pascal Venet

Received: 5 May 2024
Revised: 4 June 2024
Accepted: 8 June 2024
Published: 13 June 2024

Correction Statement: This article has been republished with a minor change. The change does not affect the scientific content of the article and further details are available within the backmatter of the website version of this article.

Copyright: © 2024 by the author. Licensee MDPI, Basel, Switzerland. This article is an open access article distributed under the terms and conditions of the Creative Commons Attribution (CC BY) license (https://creativecommons.org/licenses/by/4.0/).

1. Introduction

Lithium-ion (Li-ion) batteries are one of the most widely used rechargeable batteries in the world. Compared to other traditional secondary batteries, e.g., lead–acid, nickel–cadmium, and nickel–metal hydride batteries, Li-ion batteries exhibit higher operating voltages, higher energy density, less self-discharging, and lower maintenance requirements [1–3]. Recently, the International Energy Agency (IEA) reported that electric vehicle (EV) markets have shown exponential growth, as sales exceeded 10 million in 2022. A total of 14% of all new EVs sold were electric in 2022, up from around 9% in 2021 and less than 5% in 2020. The EV Li-ion battery demand increased by about 65% to 550 GWh in 2022 from about 330 GWh in 2021 [4]. Advancements in renewable energy supply and EV industries have enhanced the application of Li-ion batteries from small-scale 3C (computing, communication, and consumer) products [5,6] to large-scale battery energy storage systems (BESSs) [7–9] and high-power mobile energy sources.

The installation of a grid-scale Li-ion battery (100 MW, 129 MWh from Tesla and Neoen) in South Australia in 2017 has demonstrated the capability of batteries in electric grid stabilization [10,11]. After several weeks, when the Loy Yang coal-fired power plant in Victoria failed, leading to a power shortage, the backup Li-ion battery connected and sent about 100 MW into the grid within 140 ms [12,13], responding even more quickly than the coal-fired backups that were supposed to provide emergency power. These types of shock-emitting and shock-absorbing capacities help us to avoid blackouts that would otherwise occur. Batteries can provide inertia services and rapid frequency responses

(e.g., frequency control ancillary services, FCAS) to the grid, paving the way for potential regulatory modifications and revenue streams to incentivize further grid-scale energy storage systems (ESSs) [14–16]. In its first year, the grid-scale Li-ion battery facility saved nearly USD 40 million as well as helped to balance and stabilize the region's unstable grid. Large-scale battery systems have shown that they will play an important role in supplying electric networks.

Energy supply on high mountains remains an open issue to be solved. Grid connection is impractical, since the establishment and maintenance costs are too high. On the other hand, there are many environmental problems, such as the destruction of the natural ecology on the mountain. Diesel generators have been energy suppliers on high mountains for a long time despite their air pollution and noise problems. Owing to the development of renewable energy (such as solar, wind, and water), the usage of diesel generators is reduced, lowering the emissions of greenhouse gases (GHGs) [17–19]. However, most renewable energy sources possess intermittent features due to their fluctuating nature. To deal with the problem of renewable energy intermittency, ESSs are necessary [20,21]. In the past, lead–acid batteries were heavily used as ESSs, accompanied by many environmental issues, e.g., poisoning, leaks, contamination of the environment, and damage to the ecosystem [22,23]. Recently, Li-ion batteries, as a greener alternative, have started to replace lead–acid batteries in ESSs.

Since 2016, an off-grid photovoltaic (PV) ESS has been installed in Paiyun Lodge, the highest mountain lodge in Taiwan (as shown in Figure 1). In the system, solar panels provide intermittent energy generation, and the Li-ion battery ESS serves as an energy reservoir. In 2020, a system aging estimation project on the long-term usage of the solar panels and ESS was initialized, reporting that the whole system is aging but that most of the system remains healthy for long-term usage. Some repair and optimization suggestions were given in 2021. In 2022, we completed an electric power improvement project dealing with system aging problems.



Figure 1. Paiyun Lodge, the highest lodge in Taiwan, is at an altitude of 3402 m (11,161 ft), located 2.4 km (1.5 mi) below the western slope of the main peak of Mt. Jade. Photographer: Yu-Chun Lin.

The research methodology scheme of this work, divided into three parts, is shown in Figure 2. In the first part (Section 2), the energy data of the Li-ion battery system for four years are analyzed. The analysis of such massive data is not an easy task (more than 7 million rows). In particular, the data are recorded during the actual operation instead of obtaining regular data from cycle life tests in the laboratory. A method is established for analyzing the energy data during operation, including daily operation patterns, as well as the C-rate, temperature, and accumulated energy distributions, and estimating the health of

the Li-ion battery system. In the second part (Section 3), the status and problems of the old electric power system in Paiyun Lodge are described. The engineering status of the electric power system is reported, including (1) the reform and optimization of existing Li-ion battery cabinets, (2) PV inverter system reformation and optimization, (3) the reorganization of distribution boxes and power line adjustment, (4) the installation of a self-developed cloud energy management system (EMS) to remotely monitor the off-grid PV ESS. In the third part (Section 4), a simple cost model is built for comparing costs between lead–acid and Li-ion battery systems. This model reasonably explains that expensive Li-ion batteries can compete with cheap lead–acid batteries for long-term usage on high mountains. Above all, this study gives engineers and researchers a fundamental understanding of a real case of the long-term usage of off-grid PV ESSs on high mountains.

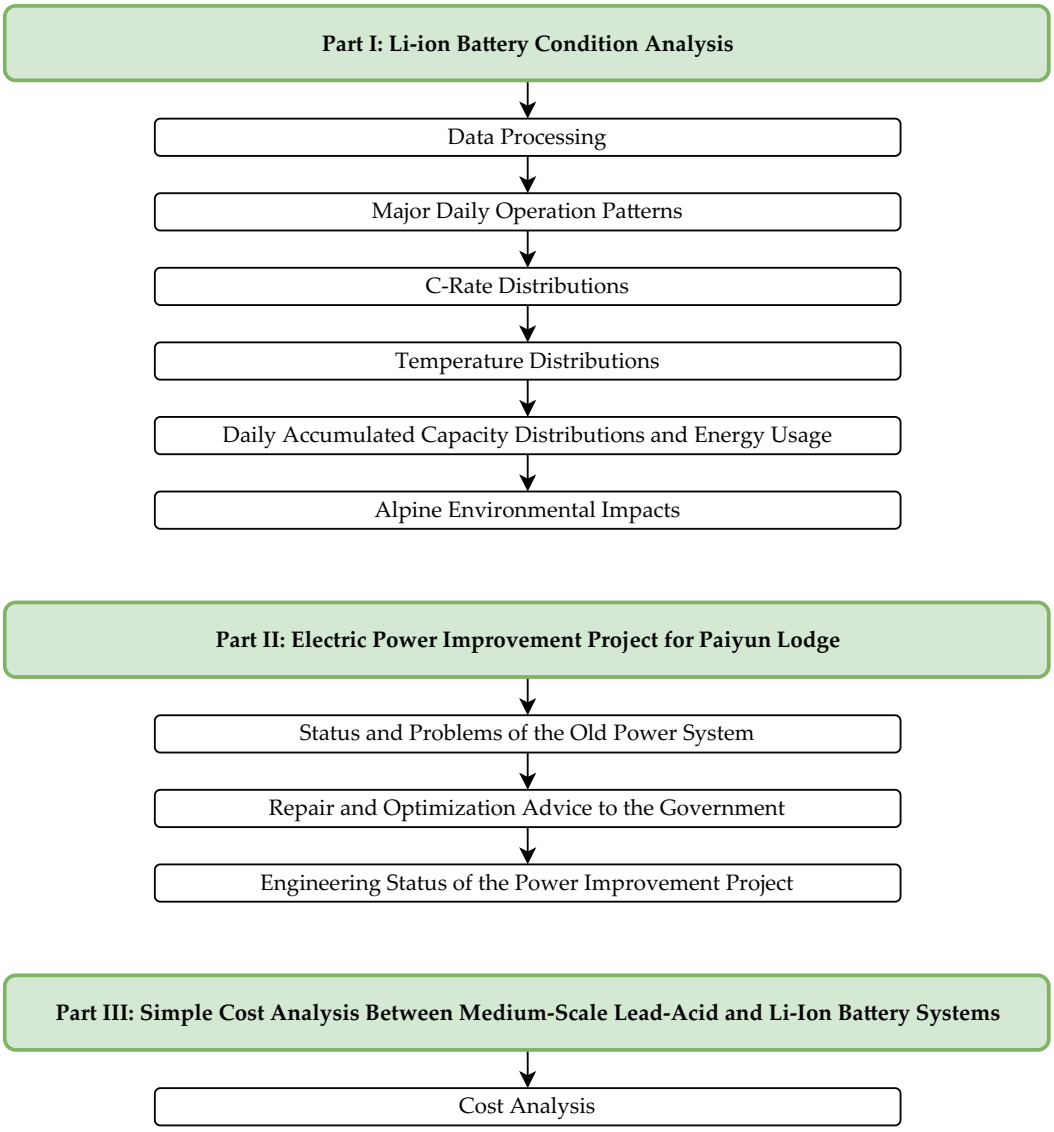


Figure 2. Methodology scheme of the work. The scheme consists of three parts: part I: Li-ion battery condition analysis; part II: electric power improvement project for Paiyun Lodge; and part III: simple cost analysis between medium-scale lead–acid and Li-ion battery systems.

2. Li-ion Battery Condition Analysis

The Li-ion battery system, with a nominal voltage of 48 V and capacity of 250 Ah, is made with a 16S5P configuration, i.e., 5 batteries connected in parallel as a group and 16 groups of batteries connected in series as a whole battery system. For long durability and thermal stability, lithium iron phosphate (LFP) batteries are chosen as battery cells

in the system [24–29]. The data were obtained from the battery management system (BMS) [30–32], including the total voltage (V_{tot}), 16 cell voltages ($V_n, n = 1 \sim 16$), the current (I), and 4 temperatures ($T_n, n = 1 \sim 4$). The data were recorded from 14 October 2016 to 20 July 2020 (about 1376 days across 5 years). There are over 7 million rows of data with data time intervals of about 15 s. In the following subsections, the data processing, major daily operation patterns, C-rate distribution, temperature distribution, capacity distribution, and energy usage of the battery system are discussed.

2.1. Data Processing

Data processing is crucial before data analysis. The data obtained from the BMS are stored in a CSV (comma-separated values) file every day. There are about 1400 CSV files in the data storage. The time duration between data points is about 15 s. The accuracy of the data and time plays an important role in data processing. If the time is obtained from the standalone BMS without network calibration, the timeline of the data should be checked first. In this case, the time was obtained based on a passive device (i.e., a crystal oscillator), and there was no network connected for time calibration once a day or once a week. After drawing the first and last CSV files, a huge time shift of about 15,000 s was found.

It is difficult to deal with 1400 CSV files one by one manually, e.g., using Microsoft® Excel v16.0 (Redmond, WA, USA) or some lightweight scientific drawing software. In this work, MathWorks® MATLAB R2022b (Natick, MA, USA) was used. The first step was to combine the data in 1400 CSV files, i.e., put all datasets into a single database. Then, a daily colormap was drawn to see the time-shift condition. Because of the daily routine operation of the ESS, the data are predicted to exhibit a roughly daily pattern on a large time scale. The time-shift issue can be solved by adjusting the time until the data exhibit a roughly daily pattern. As shown in Figure 3a, the time shift caused an obvious pattern shift in total voltage. In January 2017, the red region began at about 8 o'clock, while in July 2020, the red region began at about 12 o'clock. The time shift was a continuous process, with the red region forming the shape of a parallelogram. The red line on the left side of the parallelogram can serve as an indicator of the time shift. The more sloping the red line is, the more serious the time shift is. Some data on the right side were shifted to the left side (indicated by the red rectangle). The time-shift issue can be solved by linear adjustment, as shown in Figure 3b. The red region becomes a rectangle, indicating a roughly daily pattern. A three-dimensional (3D) plot showing the variation in the total voltage is given in Figure 3c.

Other technical suggestions for efficient large-scale data processing are given. (1) Use the parallel computing technique. In this study, 12 cores in the CPU were used simultaneously for data calculations. (2) Use programmable drawing software. There are about 1400 figures in this work. A program was written to perform batch drawing, instead of drawing figures one by one manually.

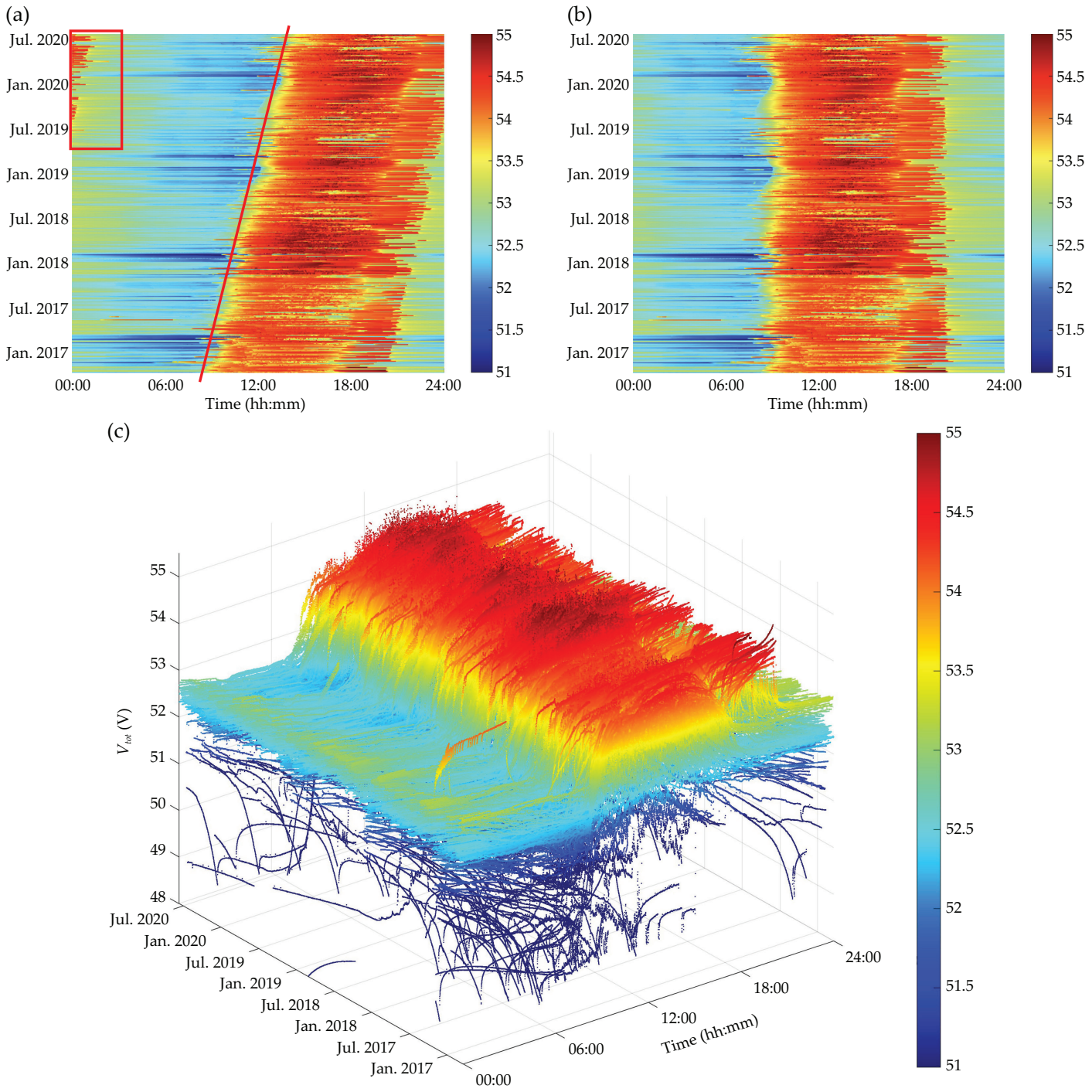


Figure 3. Data processing. (**a**) A colormap of the total voltage obtained from the source data. The oblique red line indicates a time shift (about 15,000 s) in the source data, causing a serious data shift. It is obvious that the data in the red rectangle should be on the right side of the figure. (**b**) A colormap of the total voltage obtained from the time-adjusted data. After the time adjustment, the data exhibit a clear daily pattern. (**c**) A 3D plot of total voltage obtained from the time-adjusted data.

2.2. Major Daily Operation Patterns of the Battery System

It is difficult to look at such a huge amount of data (over 7 million rows) in detail. In particular, the data obtained from real cases are not similar to the data from professional instruments. There is no explicit constant current (CC) discharge mode or constant current–constant voltage (CC-CV) charge mode for analysis [24,33]. We need some analytical skills. Looking at the data in units of days, we found that there are several major daily operation

patterns. These major patterns are highly related to the amount of solar power generated and the operating conditions of the diesel generators, as shown in Table 1. There are three solar power conditions (high, medium, and low) and two generator conditions (ON/OFF). For example, major pattern 1 is characterized by high solar power with the generator OFF.

Table 1. Conditions for the major daily operation patterns of the battery system. Four major daily operation patterns are listed based on various conditions of solar power and the generator.

	Generator OFF	**Generator ON**
High solar power	Pattern 1	No major pattern
Medium solar power	Pattern 2	Pattern 3
Low solar power	No major pattern	Pattern 4

The massive data exhibit daily patterns. Four major daily patterns are observed during system operation (while not all conditions exhibit explicit patterns). Selected data used as example cases are illustrated in Figure 4. For pattern 1 (high solar power with the generator OFF), the total voltage (V_{tot}) of the battery system exhibits a smooth curve with a bump in the daytime (Figure 4a). During the nighttime (about 17:00–09:00), no solar power is generated. The battery system is in the discharge state with a current (I) of about 5 A (Figure 4c). V_{tot} and V_{cell} gradually decrease (Figure 4a,b). During the daytime (about 09:00–17:00), the generated solar power is sufficient for the load and the battery system. The battery system is in the charge state with I at a maximum of ∼20 A (Figure 4c). V_{tot} and V_{cell} gradually increase to values of 54.5 V and ∼3.4 V, respectively (Figure 4a,b). V_{tot} varies within the safe operating range of about 48–56 V, and V_{cell}s vary within the safe operating range of LFP battery cells, which is about 3–3.5 V [24,25]. Some small voltage drops in V_{tot} and V_{cell} are due to the instantaneous high power consumption of the load (red circles in Figure 4a,b), which can be verified by the large I at the corresponding time (red circle in Figure 4c).

For pattern 2 (medium solar power with the generator OFF), as shown in Figure 4e–h, the voltage and current behaviors during the nighttime are in the discharge state and the same as those of pattern 1. During the daytime, the generated solar power is sufficient for the load, but not sufficient for the battery system. The battery system is still in the charge state, while many instantaneous current and voltage drops are observed (green circles in Figure 4e–g), reflecting the intermittent power generation characteristics of renewable energy. For pattern 3 (medium solar power with the generator ON), as shown in Figure 4i–l, the voltage and current behaviors are similar to those of pattern 2. During the daytime, insufficient solar power cannot fulfill the requirements of the battery system, and many instantaneous current and voltage drops are exhibited in the charge state (Figure 4i–k). To solve the energy shortage, the backup generator is turned on with a constant charge current of about 18 A (blue circle in Figure 4k), and the voltage is gradually charged to saturated values (blue circles in Figure 4i,j).

For pattern 4 (low solar power with the generator ON), as shown in Figure 4m–p, the voltage and current exhibit a gradual decrease with a large bump. During the daytime, low or no solar power is generated, causing the battery system to remain in the discharge state: i.e., the voltage gradually decreases (Figure 4m,n), and the current is around 5 A (Figure 4o). Later, the backup generator is turned on to charge the battery system. The battery system operation patterns give us a convenient way to recognize several normal operation modes of the battery system and quickly identify abnormal conditions.

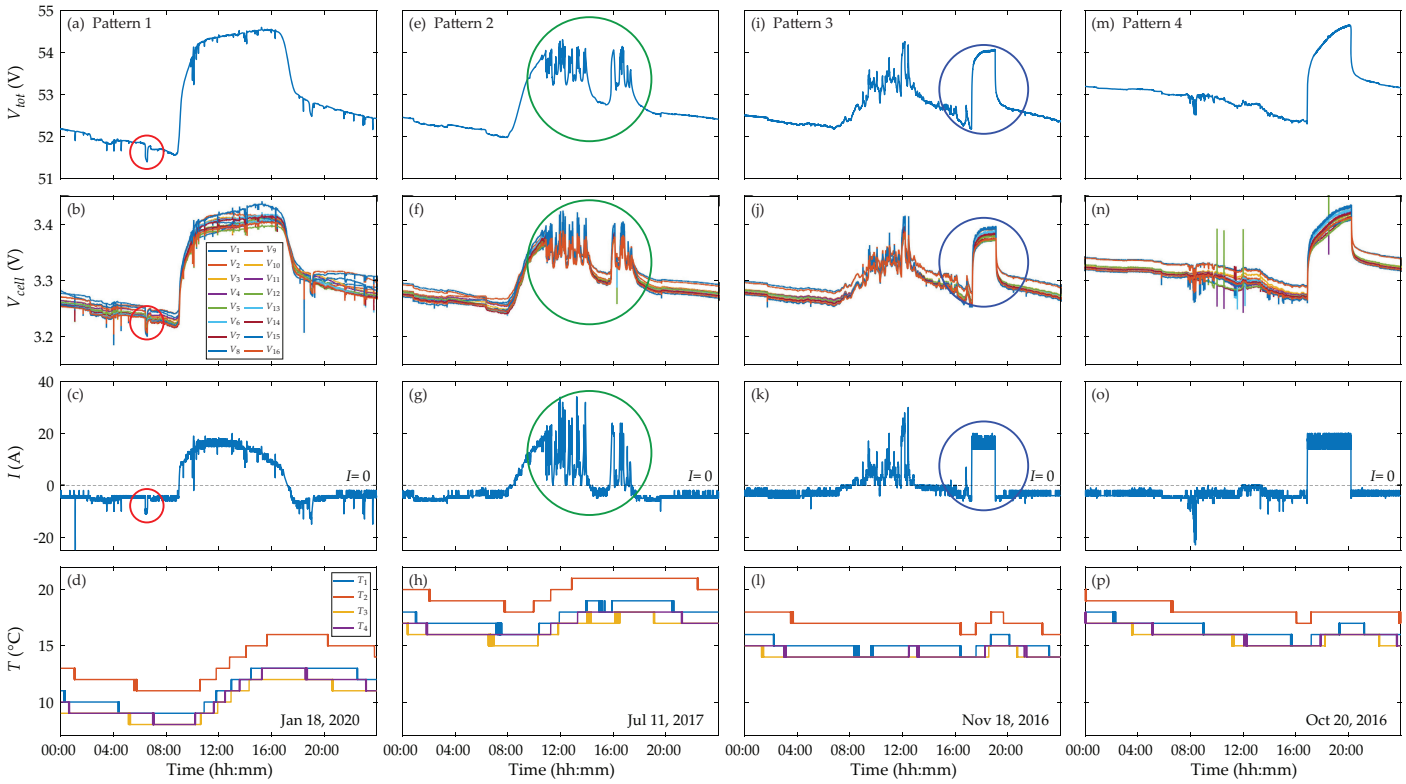


Figure 4. Four major daily operation patterns of the battery system (corresponding pattern conditions are listed in Table 1). Patterns 1, 2, 3, and 4 are shown in (**a–d**), (**e–h**), (**i–l**), and (**m–p**), respectively. Each pattern contains the total voltage (V_{tot}), 16 cell voltages ($V_n, n = 1{\sim}16$), the current (I), and 4 temperatures ($T_n, n = 1 \sim 4$). The level of zero current ($I = 0$) is denoted by dashed lines, and the charge (discharge) current is a positive (negative) value. The red circles highlight the instantaneous voltage drop and high current of the battery system. The green circles highlight many instantaneous voltage and current drops under the charge state of the battery system. The blue circles mark the characteristic voltage and current variations caused by the diesel generator. The date is displayed in the lower-right corner of each pattern.

2.3. The C-Rate Distribution of the Battery System

The C-rate (C_R) is one of the key and simple factors in analyzing the charge and discharge conditions of the battery system, where $C_R \equiv I/Cap_N$ is the current I per unit of nominal ampere-hour capacity Cap_N [24,34]. The current is usually expressed in terms of the C-rate, i.e., the current normalized to the nominal capacity of the battery. The increase in charge and discharge C-rates causes ohmic heating with a rising temperature, causing Li-ion batteries to degrade faster. Chen et al. designed a calorimeter to measure the thermal behaviors of LFP prismatic batteries at $C_R = 0.25$–$3\ \mathrm{h}^{-1}$ and found that the heat generation rate increases with the C-rate [35]. Drake et al. studied the heat generation rate of a 26650 LFP battery by heat flux measurements under a discharge C-rate ranging from $C_R = 1$ to $9.6\ \mathrm{h}^{-1}$. At a high C-rate of $C_R = 9.6\ \mathrm{h}^{-1}$, the surface temperature climbed to 40 °C and even reached the temperature safety limit before finishing the entire discharge process [36]. Chung et al. found that high-C-rate charging ($C_R > 5\ \mathrm{h}^{-1}$) is unsuitable for batteries and might lead to thermal runaway and fire hazards [37]. Wu et al. investigated the relationship among the temperature, discharge C-rate, and cycle life of pouch cells. At room temperature, the larger the C-rate, the faster the capacity fade and the larger the ohmic resistance [38]. The solid electrolyte interface (SEI) layer grows with temperatures over 25 °C, leading to faster, irreversible capacity fade [33,39]. In addition to capacity fade, a high C-rate can also accelerate the aging process of cell components in a Li-ion battery and shorten the cycle life [40]. For example, the chemical composition of the surface of the current collector changes significantly [41], the decomposition of electrolytes (e.g., $LiPF_6$) is accelerated [42], and significant ethylene (C_2H_4) evolution occurs [43].

Unlike power batteries used in EVs, which have instantaneous high-power requirements ($C_R > 1\ h^{-1}$), most battery systems in stationary applications are designed to normally operate at a low C-rate ($C_R < 0.25\ h^{-1}$) with an instantaneous high-power output mode at $C_R < 1\ h^{-1}$ for safety and service life extension [44–46]. For example, the grid-scale Li-ion battery (100 MW, 129 MWh from Tesla and Neoen) was installed in Hornsdale, South Australia, in 2017 [10,11]. When the Loy Yang coal-fired power plant in Victoria failed as backup energy storage for the grid, leading to a power shortage, a power of 100 MW was input into the national electricity grid within 140 ms [12,13]. In this case, the instantaneous output C-rate was about 0.78 h^{-1}. For the discussed battery system, the time distribution of the C-rate during battery system operation is shown in Figure 5. Almost all values (over 99.9%) of the C-rate during charging are under 0.1 h^{-1}, and more than 70% of the time, they are at $C_R < 0.01$. On the other hand, the C-rate during discharging is almost always under 0.05 h^{-1}, and over 95% of the time, it is at $C_R < 0.03$. The battery system operates under a low-C-rate condition, with the values of the C-rate lower than the normal design C-rate, i.e., $C_R < 0.25\ h^{-1}$. The low-C-rate condition can avoid excessive voltage differences among battery cells and heat concentration on the current collectors, ensuring system stability and prolonging the life of the system.

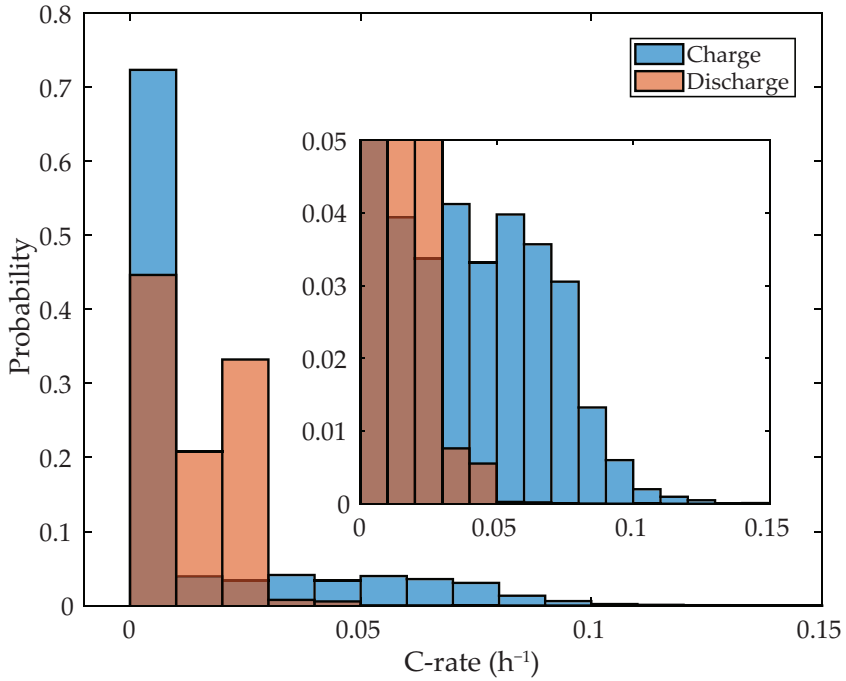


Figure 5. The time distribution of the C-rate during battery system operation. The probabilities of charge and discharge C-rates are marked by blue and red bars, respectively. The inset shows the low-probability region. The battery system operates at a C-rate $C_R < 0.15\ h^{-1}$, which is lower than the suggested value of $C_R < 0.25\ h^{-1}$, advancing system stability and prolonging the life of the system. Time range of data: 14 October 2016∼20 July 2020. (Total: 1376 days).

2.4. The Temperature Distribution of the Battery System

The operating temperature and temperature distribution have a large impact on the performance, lifespan, and safety of the battery system. The acceptable operating temperature for Li-ion batteries ranges from −20 to 60 °C [47]. To maintain better performance, a narrow temperature range of about 15–35 °C is recommended [48,49]. Temperatures outside the desired operating range will lead to fast capacity fade. Moreover, when the cell temperature exceeds the threshold of the thermal runaway point, chain electrochemical reactions might cause battery cells to burn and explode [50]. The operating temperature of the discussed battery system, ranging from 0 to 25 °C, is shown in Figure 6a. The temperature variation exhibits an annual pattern, reflecting seasonal climate characteristics,

i.e., high temperatures in summer and low temperatures in winter. More than half of the time, it is in the recommended range of operating temperatures (Figure 6c).

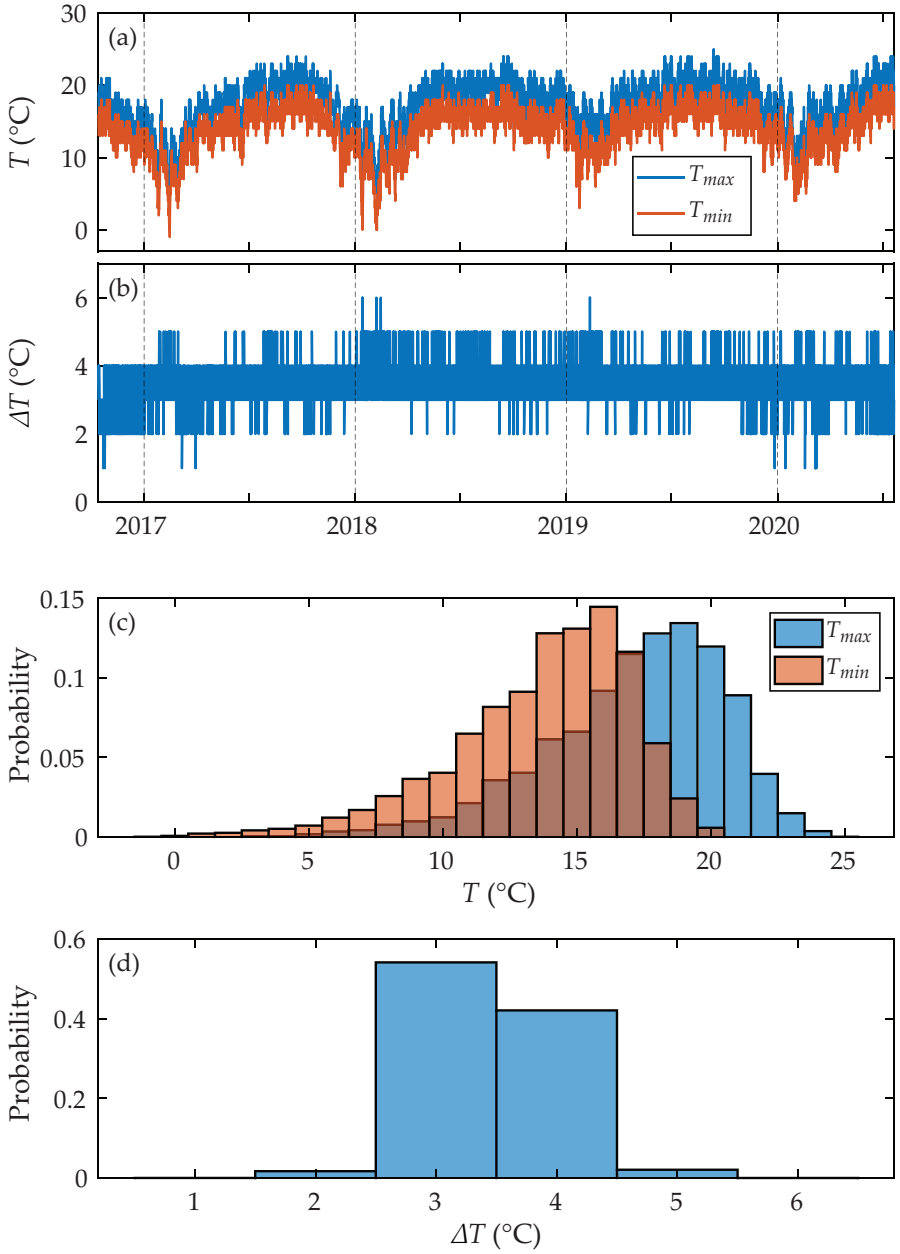


Figure 6. The temperature distribution of the battery system. (**a**) The variation in maximum and minimum temperatures over time, where T_{max} and T_{min} are indicated by blue and red curves, respectively. (**b**) The variation in the temperature difference (ΔT) over time. (**c**) The distribution of maximum and minimum temperatures. (**d**) The distribution of temperature differences. Time range of data: 14 October 2016∼20 July 2020. (Total: 1376 days).

The temperature difference ($\Delta T = T_{max} - T_{min}$) among the battery cells in a pack should be as low as possible for better performance of the battery system, where T_{max} and T_{min} are the maximum and minimum temperatures of the battery cells in the pack, respectively. Such a condition is called temperature uniformity (or thermal balance), and the desired value is less than 5 °C [51–55]. For the discussed battery system, over the whole period analyzed, ΔT is almost always under 5 °C but reaches 6 °C several times (Figure 6b). As illustrated in Figure 6d, about 95% of the time, ΔT is 3 and 4, i.e., $\Delta T < 5$°C, indicating that the Li-ion battery system has good temperature uniformity.

The temperature and C-rate are two key factors that impact the aging rate of Li-ion batteries. The aging speed can be described by aging rates, which are contained in the capacity fade curves. Arrhenius's theory [56–58], considering the effects of temperature and C-rate, has been applied in the field of Li-ion batteries to determine activation barriers for aging [59,60] and other processes [61–64]. A slope change in an Arrhenius plot indicates a mechanism change [33]. Arrhenius behavior has been observed in Li-ion batteries [60,65,66], showing a minimum aging rate at a certain temperature. This minimum in the Arrhenius plot with a certain C-rate (T = 5–25°C and $C_R < 0.2\ \mathrm{h}^{-1}$) points to the longest cycle life of Li-ion batteries [33,44]. For the discussed battery system, the aforementioned operating temperature and C-rate are close to the minimum in the corresponding Arrhenius plot, indicating a slower aging rate and longer life of the battery system.

2.5. Daily Accumulated Capacity Distributions and Energy Usage of the Battery System

The accumulated capacity (energy) is an important quantity for judging the health of batteries. The accumulated capacity can be calculated from the source data by the trapezoidal rule, which was applied in Babylon before 50 BCE for integrating the velocity of Jupiter along the ecliptic [67]. The trapezoidal rule works by approximating the region under the curve of the function $f(x)$ as a trapezoid and calculating its area. In real cases, the composite trapezoidal rule with non-uniform spacing is used for accumulating data:

$$\int_a^b f(t)dt \approx \sum_{n=1}^{N} \frac{f(t_{n-1}) + f(t_n)}{2} \Delta t_n, \tag{1}$$

where t_n is a point in the partition of $[a, b]$ ($a = t_0 < t_1 < \cdots < t_{N-1} < t_N = b$), $\Delta t_n = t_n - t_{n-1}$ is the interval, and $n = 0, 1, 2, \ldots, N$ is an integer. The accumulated capacity (C_{acc}) can be obtained by

$$C_{acc} = \int_a^b I(t)dt \approx \sum_{n=1}^{N} \frac{I(t_{n-1}) + I(t_n)}{2} \Delta t_n, \tag{2}$$

where $I(t_n)$ is the current value of the t_n point from the source data. The accumulated energy (E_{acc}) can be calculated by

$$\begin{aligned} E_{acc} &= \int_a^b I(t)V(t)dt \\ &\approx \sum_{n=1}^{N} \frac{I(t_{n-1})V(t_{n-1}) + I(t_n)V(t_n)}{2} \Delta t_n, \end{aligned} \tag{3}$$

where $V(t_n)$ is the total voltage value of the t_n point from the source data.

The daily accumulated capacity and energy usage calculated by Equations (2) and (3) are shown in Figure 7. The major probability of the daily accumulated charge capacity (C_{day}^{chg}) is distributed around 70–90 Ah, while the major probability of the daily accumulated discharge capacity (C_{day}^{dis}) is around 60–80 Ah (Figure 7a). The daily accumulated charge capacity is generally higher than the daily accumulated discharge capacity, and this feature is more obvious when we check the daily capacity loss, i.e., the difference between the daily accumulated charge and discharge capacities, $\Delta C_{day} = C_{day}^{chg} - C_{day}^{dis}$. As shown in Figure 7b, ΔC_{day} exhibits a maximum probability at around 10–20 Ah. The overall distribution of ΔC_{day} is located in the positive region, indicating that the daily accumulated input energy is higher than the daily accumulated output energy, i.e., an energy loss in the battery system. The energy loss in the battery system can be explained by the equivalent circuit model (ECM), which is the most common battery model, consisting of resistance, capacitance, and inductance elements [68–70]. The effective resistance causes joule heating during charging and discharging, resulting in energy loss in the battery system.

The daily accumulated energy, a counterpart to the daily accumulated capacity, is depicted in Figure 7c,d. Similar distributions are observed. The major probability of the daily accumulated charge energy (E_{day}^{chg}) is distributed around 3.75–4.75 kWh, while the major probability of the daily accumulated discharge energy (E_{day}^{dis}) is around 3.25–4.25 kWh (Figure 7a). The overall distribution of the difference between the daily accumulated charge and discharge energies ($\Delta E_{day} = E_{day}^{chg} - E_{day}^{dis}$) is located in the positive region, with a value of about 0.5–1 kWh, indicating energy loss in the battery system.

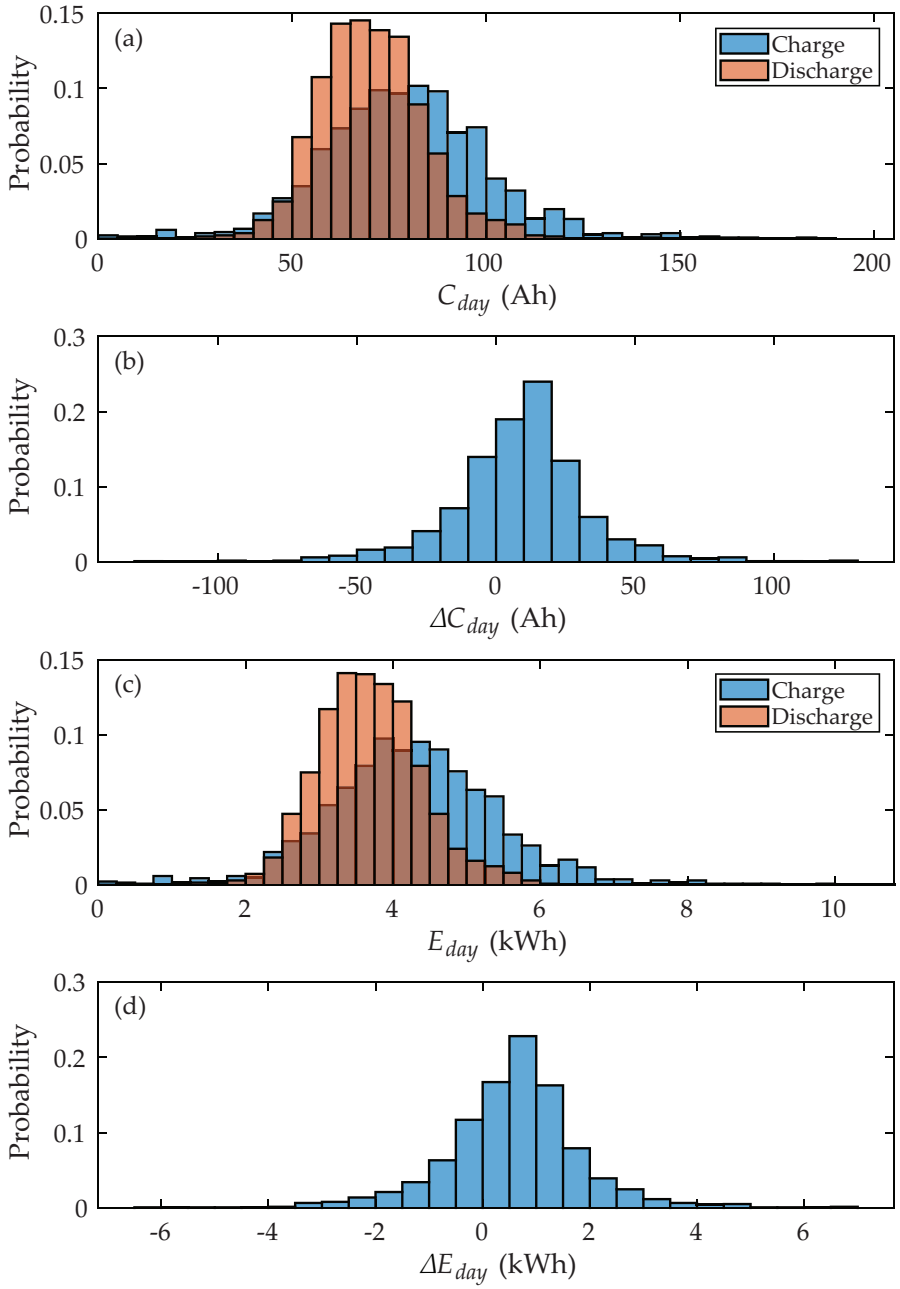


Figure 7. Daily accumulated capacity and energy distributions of the battery system. (**a**) The distribution of accumulated charge and discharge capacities, where the accumulated charge and discharge capacities are marked by blue and red bars, respectively. (**b**) The distribution of the daily accumulated capacity difference (ΔC_{day}). (**c**) The distribution of the daily accumulated charge and discharge energies. (**d**) The distribution of the daily accumulated energy difference (ΔE_{day}). Time range of data: 14 October 2016∼20 July 2020. (Total: 1376 days).

The annual data on the accumulated capacity and energy usage of the battery system are listed in Table 2. The annual accumulated charge capacity (C_{year}^{chg}) and annual accumulated discharge capacity (C_{year}^{dis}) exhibit the relationship $C_{year}^{chg} > C_{year}^{dis}$ with the scale in years. The annual capacity loss rates (CR_{year}^{loss}) calculated by

$$CR_{year}^{loss} = 100\% \times \frac{(C_{year}^{chg} - C_{year}^{dis})}{C_{year}^{chg}} \quad (4)$$

have values from 8.2 to 13.9%, and the capacity loss rate over the whole period analyzed is about 11.2%. The cycle number per year can be calculated by the discharge capacity per year over the nominal capacity of the battery system (C_{year}^{dis}/C_{nom}), where $C_{nom} = 250$ Ah is the nominal capacity of the discussed battery system. To discuss energy usage explicitly, the annual accumulated charge energy (E_{year}^{chg}) and annual accumulated discharge energy (E_{year}^{dis}) are given. The relationship $E_{year}^{chg} > E_{year}^{dis}$ with the scale in years remains. The annual energy loss rates (ER_{year}^{loss}) calculated by

$$ER_{year}^{loss} = 100\% \times \frac{(E_{year}^{chg} - E_{year}^{dis})}{E_{year}^{chg}} \quad (5)$$

have values from 11.1 to 16.3%, and the overall energy loss rate is about 13.8%.

While the battery system is operating, it is impractical to obtain the full charge and discharge capacities. Because we cannot arbitrarily shut down the system to perform CC-CV charge and CC discharge tests [24], the estimation of the battery system's capacity fade has become an open issue for the industry. Experimental results demonstrated that, at low C-rates ($C_R < 0.5$ h^{-1}), capacity fade is substantially affected by two parameters, i.e., cycle number and temperature, while the depth of discharge (DOD) has a negligible effect on capacity fade [71]. For the discussed battery system, the average cycle number per year is about 103, and the total cycle number is 387, as listed in Table 2. Compared to the data of LFP batteries (cycle life of about 2000–4000 cycles, with remaining capacity of about 80%) [45,46], the battery system is far from the end of life (EOL), with an estimated remaining capacity of more than 95%.

Table 2. The annual capacity and energy usage of the battery system.

Time Interval	C_{year}^{chg} (Ah)	C_{year}^{dis} (Ah)	CR_{year}^{loss} (%)	Cycle Number	E_{year}^{chg} (kWh)	E_{year}^{dis} (kWh)	ER_{year}^{loss} (%)
14 October 2016∼31 December	5458.6	4699.1	13.9	18.8	294.0	246.1	16.3
2017	25,434.2	23,142.9	9.0	92.6	1371.8	1212.3	11.6
2018	29,690.8	26,213.7	11.7	104.9	1606.0	1375.9	14.3
2019	31,587.8	27,270.6	13.7	109.1	1706.3	1429.6	16.2
1 January 2020∼20 July	16,804.3	15,422.9	8.2	61.7	908.0	807.1	11.1
All time	108,975.8	96,749.2	11.2	387.0	5886.1	5071.0	13.8

2.6. Alpine Environmental Impacts on Battery Systems

The impact of alpine environmental characteristics on battery systems can be evaluated from the perspective of two major physical quantities, i.e., temperature and pressure. In terms of temperature, if the battery is placed outdoors, it may be too low, making it difficult to charge and discharge the battery. Outdoors, there is also the problem of the excessive temperature difference between day and night, which will cause the battery life to be shortened. If the battery is placed indoors, in a well-insulated environment, and combined with the heat generated by the operation of other equipment, the battery temperature may be moderate, and there will be no problems caused by the excessive temperature difference between day and night. For example, the ESS in Paiyun Lodge is located indoors. In terms

of pressure, the air pressure in high mountains is low, which will cause expansion problems for soft-packed batteries. Another point is the opening pressure of the battery safety relief valve. Since the valve opening pressure is designed for use on flat ground, moving to a mountain with a lower outside air pressure and external pressure drops may cause the valve to open prematurely.

3. Electric Power Improvement Project for Paiyun Lodge

In this section, the status and problems of the old power system in Paiyun Lodge are described first. Then, some repair and optimization advice is listed. Finally, the entire status of the electric power improvement engineering project and other issues are stated.

3.1. Status and Problems of the Old Power System in Paiyun Lodge

The power architecture of the old system in Paiyun Lodge (comprising energy creation, energy storage, and energy consumption) is shown in Figure 8a. The energy flows related to direct current (DC) and alternative current (AC) are colored in green and red, respectively. To avoid confusion between the DC and AC systems, the subscripts of some units will add DC or AC to differentiate between them, e.g., V_{DC} indicates DC voltage. For energy creation, the first, second, third, and sixth PV arrays, with a total solar capacity of 7.8 kW_p, were installed before 2016. After passing through the maximum power point trackers (MPPTs), the power directly enters the Li-ion battery ESS. The fourth and fifth PV arrays, with a total solar capacity of 4.8 kW_p, were installed after 2016, and their power is passed to the ESS by hybrid solar inverters. A diesel generator is used as a backup and emergency power source for the hybrid solar inverters. Energy storage is provided by a 48 V_{DC} Li-ion battery ESS (composed of six battery cabinets with a total capacity of 72 kWh). For energy consumption, the 220 V_{AC} power is mainly provided by the hybrid solar inverters and is converted into 110 V_{AC} power by the step-down device, and then power is supplied to the loads of Paiyun Lodge, the medical station, and the base station.

On the roof of the lodge are the 1st–6th PV arrays with solar capacities of 2 kW_p, 2 kW_p, 2 kW_p, 2.4 kW_p, 2.4 kW_p, and 1.8 kW_p, respectively. The major equipment and distribution boxes are located in the machine room, as shown in Figure 9. The ESS, composed of six Li-ion battery cabinets, is indicated by boxes in green color. Each Li-ion battery cabinet is made of a battery pack with a nominal voltage of 48 V_{DC} and a BMS. The 48 V_{DC} battery pack is composed of LFP batteries with a 16S5P configuration; in other words, there are five battery cells connected in parallel as a group and 16 groups of battery cells connected in series as a whole battery pack of 80 battery cells. Each battery cell possesses a capacity of 50 Ah, and the capacity of each cabinet is about 12 kWh. The entire capacity of the ESS is about 72 kWh. Three hybrid solar inverters are on the wall, with a maximum output power of 15 kW (blue boxes in Figure 9). Seven distribution boxes are on the wall, connecting the PV arrays, hybrid solar inverters, old MPPTs, old inverters, generator, transformer, and loads (red boxes in Figure 9).

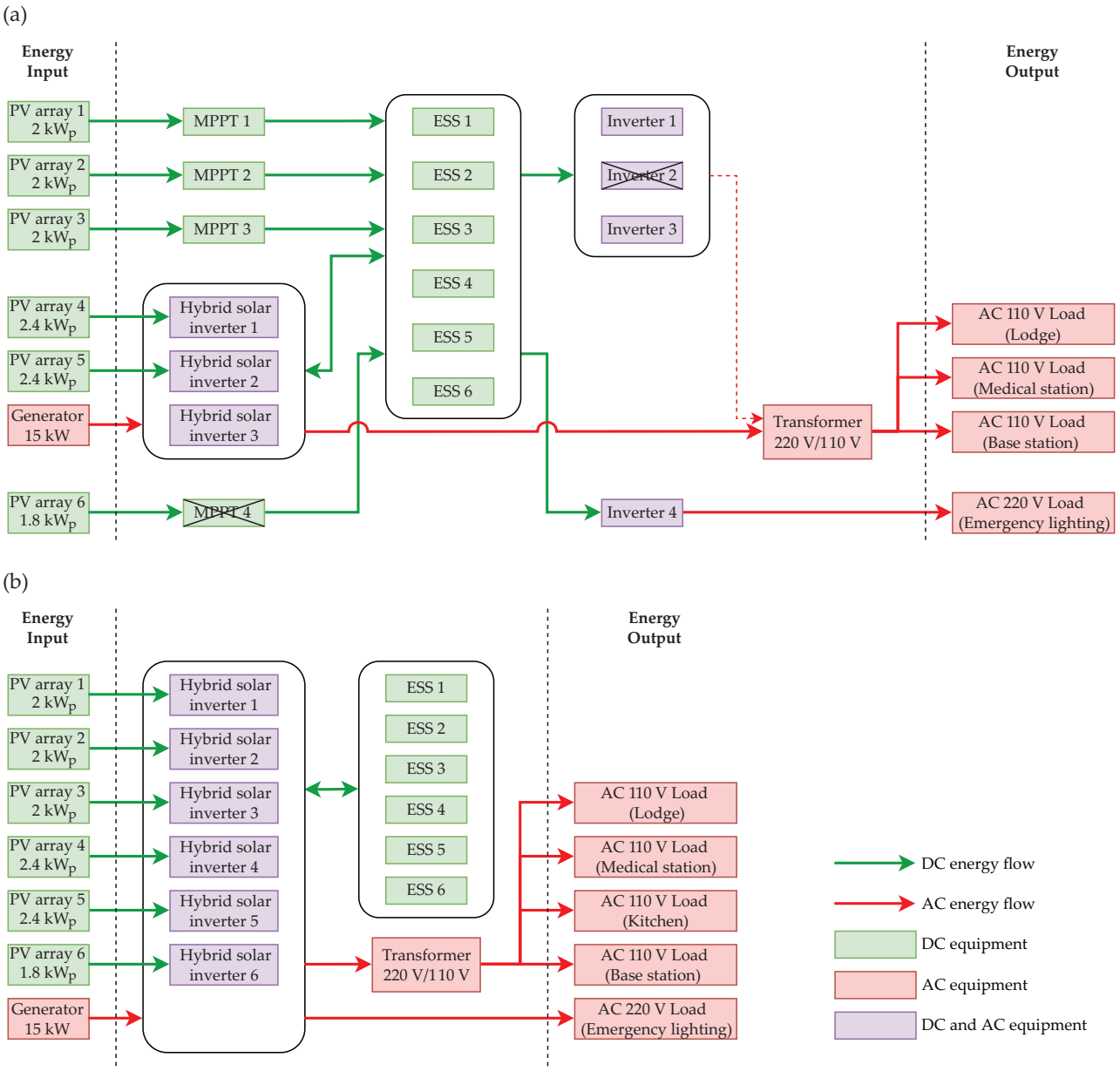


Figure 8. The electricity architecture of the old and improved power systems in Paiyun Lodge. (**a**) In the old power system, the DC power generated by the 1st, 2nd, 3rd, and 6th PV arrays is sent to the ESS by the 1st–4th MPPTs and is then converted to 220 V_{AC} power by the 1st–4th inverters. The transformer converts the AC power from 220 V_{AC} to 110 V_{AC} for general purposes (i.e., Paiyun Lodge, medical station, and base station). The 220 V_{AC} power for emergency lighting is directly obtained from the 4th inverter. The rounded rectangles indicate that the devices work in parallel. Since 2016, electricity for general purposes has been provided by another power system, and the ESS has changed from lead–acid batteries to Li-ion batteries. The DC power generated by the 4th and 5th PV arrays is sent to the ESS by the 1st and 2nd hybrid solar inverters and is then converted to 220 V_{AC} power by the 1st–3rd hybrid solar inverters. The 15 kW generator serves as backup power for the system. The 2nd inverter and the 4th MPPT failed. (**b**) In the improved power system, the DC power generated by the 6 PV arrays is sent to the ESS by the 6 hybrid solar inverters, and the converted 220 V_{AC} power is sent directly to the load for emergency lighting and sent to the load for general purposes by the transformer. The electricity architecture and energy flow become simplified. The green and red arrows indicate the DC and AC energy flows, respectively. The green, red, and purple boxes indicate DC, AC, and DC/AC equipment, respectively.

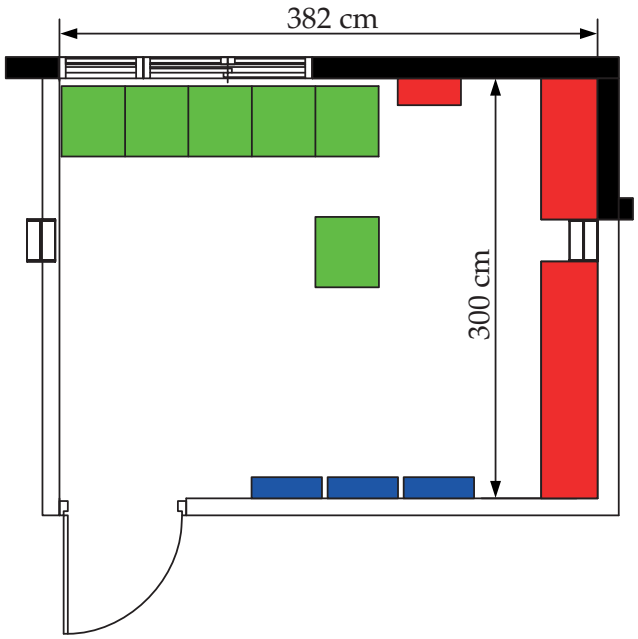


Figure 9. A map of the machine room (unit: cm). The 48 V_{DC} Li-ion battery ESS, composed of 6 Li-ion battery cabinets with a total energy of 72 kWh, is indicated by green boxes. Three hybrid solar inverters on the wall, with a maximum output power of 15 kW, are indicated by blue boxes. Seven distribution boxes on the wall connecting energy input and output systems are indicated by red boxes.

Several problems with the old power system are listed below.

1. **Long-term operation causes system aging.** The off-grid PV ESS of Paiyun Lodge was installed in October 2016, and it has entered its seventh year of operation. In the past seven years, the system has been working 24 h a day without interruption, and the aging of equipment is inevitable. In particular, the aging of the semiconductor components in the inverter is more obvious, which has gradually caused the system to stop without warning from time to time. It must be restarted before the system can be used again. This is a warning sign that the hybrid solar inverters need to be replaced to avoid the system further deteriorating into a more serious condition. In addition, once a fault occurs, the system will be shut down for a long time. Whether it is an MPPT or a hybrid solar inverter, it has been operating for more than 6 years. Among them, the MPPT was installed 17 years ago. These devices are already discontinued products. Failing to repair them will lead to difficult and time-consuming work. It might take several months to half a year to receive the devices from the manufacturer, which means that the system will be shut down for a long time.
2. **Imbalance of battery voltages in the energy storage cabinet and some faulty batteries.** After seven years of operation, the Li-ion batteries have entered a state of imbalanced battery voltages. In the past few years, it has been found that the situation is becoming more and more serious. In addition, some batteries have been in very poor condition and are judged to be faulty, which has seriously affected the overall operation of the system.
3. **Overly complex power paths to the ESS.** The power path complexity of the ESS is increased by having two kinds of power paths. The path "charge and discharge through different ports" is used for the power input of the 1st–4th MPPTs and the power output of the 1st–3rd inverters. The path "charge and discharge through the same port" is used for the 1st–3rd hybrid solar inverters. When installing another power system in 2016, the power paths of the two systems were combined in the Li-ion battery ESS to expand the solar power capacity. This situation increases the

power path complexity of the ESS, with a consequent increase in the probability of system failure.

4. **Idle solar panel for older systems.** The power of the sixth PV array cannot be used due to the failure of the fourth MPPT (as shown in Figure 8a), and solar energy of 1.8 kW_p is wasted.

3.2. Repair and Optimization Advice to the Government

A proposal consisting of repair and optimization advice was made in 2021. Some points are listed below.

1. **Replace hybrid solar inverters and integrate PV power paths.** The power of all PV arrays directly passes through the hybrid solar inverters and then goes to the Li-ion battery ESS. By replacing the hybrid solar inverter with a new version, the maintenance problem of the system can be solved, and the system can be prevented from shutting down for a long time. In addition, the power of the sixth PV array could be used again by the new hybrid solar inverter; the power can be reconnected to the lodge for use, increasing the energy supply of the lodge.
2. **Reduce the power path complexity of the ESS.** By replacing the hybrid solar inverters, two kinds of power paths will become one (i.e., "charge and discharge in the same port"), reducing the complexity of the power path and failure possibility.
3. **Replace new batteries and install an active voltage balancer.** Replacing the faulty Li-ion batteries resolves the influence of the Li-ion battery ESS. On the other hand, active balancers are installed for the ESS to actively balance the voltage of the unbalanced batteries, prolong the service life of the batteries, and improve the system stability.
4. **Construct a cloud EMS.** The energy input, output, and battery conditions of the entire off-grid PV ESS can be monitored. The relevant data are stored in the cloud database so that remote engineers can know the real-time status of the system and perform pre-processing before the system has obvious problems to avoid serious incidents, maintain system health, and improve system usage. At the same time, the EMS can also provide statistical data on energy use, annual total power generation, annual total power consumption, etc., for the competent unit to evaluate the energy usage status.

3.3. Engineering Status of the Power Improvement Project

The engineering project started on 29 July 2022, and the scheduled completion date was 26 October 2022. The approved construction period was 90 calendar days. The project was completed on the 77th calendar day of the cumulative construction period (13 calendar days in advance), as shown in Figure 10. The project status is described below.

Reform and optimization of existing Li-ion battery cabinets. This step includes replacing old and faulty batteries and installing active balancers. In determining the replacement of old and faulty battery cells, if the appearance is obviously swollen or there is leakage or voltage in an abnormal range, the battery should be replaced. Each 48 V_{DC} energy storage cabinet is made of a 16S5P configuration. All battery modules were removed from the battery cabinet for checking, as shown in Figure 11. The fourth energy storage cabinet has three groups of battery cells that have swelled significantly and have abnormal voltages of 1.000 V_{DC} and 0.967 V_{DC}. (For an LFP battery cell, the normal operating voltage is about 2.5–3.65 V [24,25].) Each group of battery cells needs to be replaced with 5 battery cells, for a total of 15 cells. The fifth energy storage cabinet has two groups of battery cells that are obviously swollen, and each group of battery cells needs to be replaced with 5 battery cells, for a total of 10 cells. Overall, a total of 25 batteries were replaced. An LFP battery cell with a capacity of 50 Ah is used in the replacement, which is made by Chang Hong Energy Technology Co., Ltd., Taiwan.

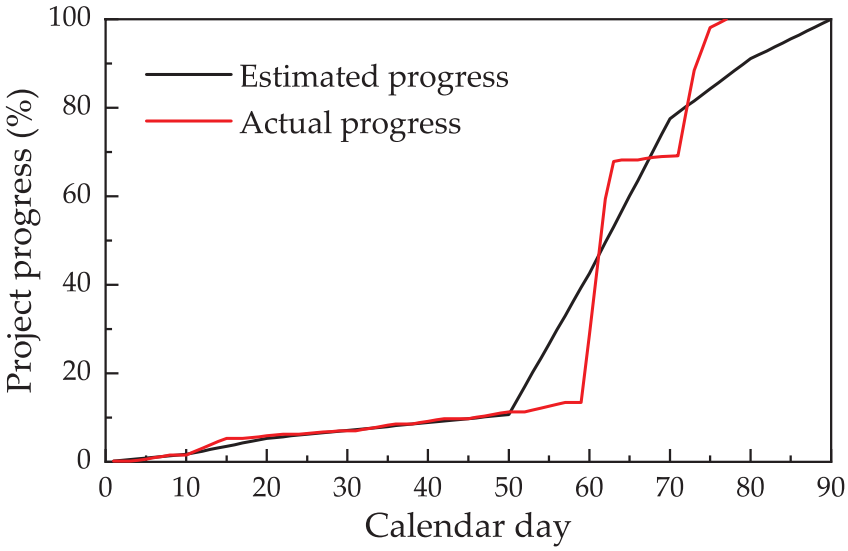


Figure 10. An S-curve of the project. The estimated progress and actual progress are indicated by the black and red curves, respectively. The project was completed 13 calendar days ahead of schedule.

Installation of active balancers to solve the problem of large voltage differences among battery groups. The active balancer with a maximum balancing current of 10 A is used. Compared with a 250 Ah battery, the maximum charge and discharge current of 10 A corresponds to $C_R = 0.04\ h^{-1}$, which means that the balance current should be used to balance the voltage without causing a large voltage drop or rise. During installation, measuring the balance current between two adjacent battery groups is one of the important checkpoints. A non-zero balance current indicates that the active balancer works well. Since the balance current is small, it requires 1 to 2 days to observe the condition after installing the active balancers. The average voltage differences (ΔV_{avg}) during charging for all energy storage cabinets drop below 60 mV (as shown in Table 3). ΔV_{avg} shrinkage is an effective way to expand the available capacity of the old Li-ion battery ESS. Furthermore, voltage balancers can effectively avoid overcharging and overdischarging the battery, effectively prolonging the battery life [72]. As one energy cabinet undergoes reform and optimization, the remaining five cabinets still operate and provide the lodge with uninterrupted electricity.

Solar inverter system reformation and optimization. Four MPPTs, four inverters, and three hybrid solar inverters of the old power system are dismantled (Figure 8a). In the improved system, six new-version hybrid solar inverters are installed, as shown in Figure 8b. The electricity of the six PV arrays enters the six hybrid solar inverters. All inverters will operate in parallel mode and output one-phase two-wire (1P2W) 220 V_{AC} power at 60 Hz. The 220 V_{AC} power is sent directly to the load for emergency lighting and sent to the load for general purposes through the 220 V_{AC}/110 V_{AC} transformer. Because maintenance and protection are not easy on high mountains, they will be handled by over-installation. Six hybrid solar inverters can disperse the load of the lodge. As one inverter fails, the other five can still operate, and the load of the surviving inverters will increase by about 20% each. If this happens in the old system, the increase in load is about 50%. Hence, over-installation can effectively improve the working stability of the system. In addition, it is time-consuming work to install six hybrid solar inverters at once. There is a key to reducing the outage time. In the early stage, we can install two hybrid solar inverters to provide temporary electricity. After the other four hybrid solar inverters are installed on the wall, all inverters can come back online at once.

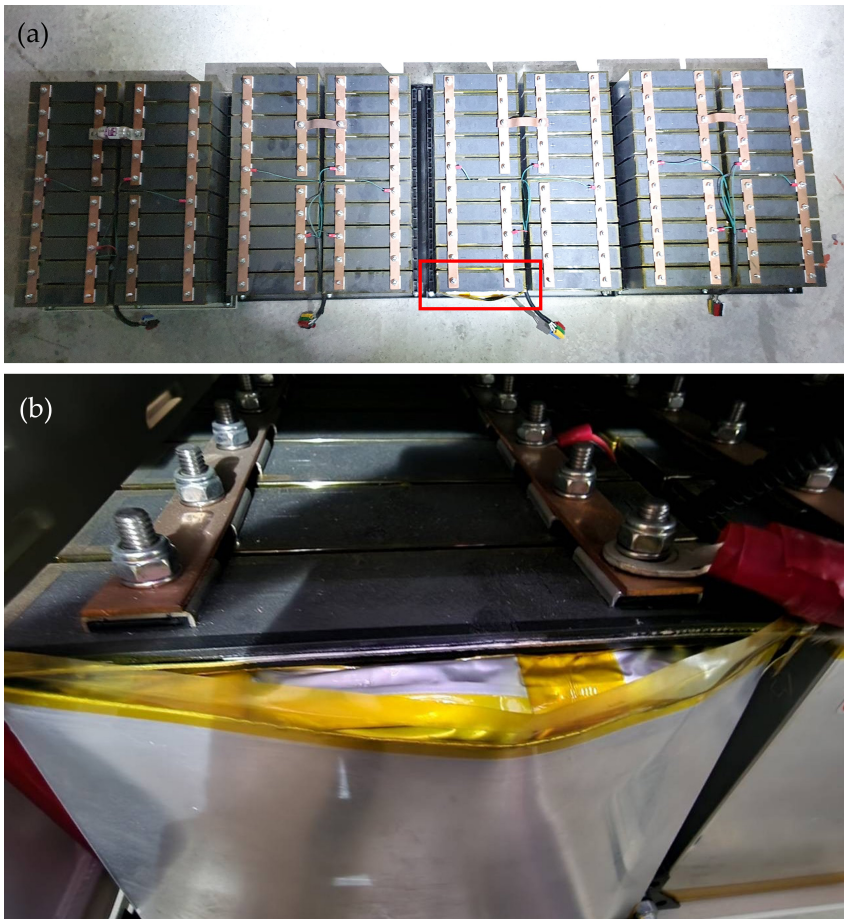


Figure 11. (**a**) Removing all battery modules from the battery cabinet and checking the appearance and voltages. Taking this energy storage cabinet as an example, there are 16 strings of battery cells, and each string is connected in parallel with 5 battery cells, for a total of 80 battery cells. Swollen battery cells are marked by the red rectangle. (**b**) Swollen battery cells should be replaced.

Table 3. Average voltage differences ΔV_{avg} during charging before and after installation of active balancers. With active balancers, ΔV_{avg}s drop below 60 mV.

Cabinet No.	ΔV_{avg} (mV) without Balancers	ΔV_{avg} (mV) with Balancers
1	163	38
2	124	57
3	153	20
4	2552 *	37
5	152	21
6	34	26

* The value of ΔV_{avg} is very large due to the low voltages of the faulty battery cells.

Reorganization of distribution boxes and power line adjustment. The power lines of old and abandoned systems have been removed for safety. Distribution boxes as power connections and breakpoints have been reorganized, and the number of distribution boxes has been reduced from 9 to 7, indicating that the power lines have become simpler. Four distribution boxes connect hybrid solar inverters directly, i.e., one controlling the input power from PV arrays, one controlling the input/output power from the ESS, one controlling the 220 V_{AC} input power (power from the generator), and one controlling the 220 V_{AC} output power. Such an organization can physically separate hybrid solar inverters from PV arrays, the ESS, the generator, and the AC power output. If one or several inverters fail, the failed part can be physically separated for repair, and the remaining parts of the

system can still operate and provide electricity. There are three distribution boxes for power output. One is for the transformer converting power from 220 V_{AC} to 110 V_{AC}. One controls the 110 V_{AC} power for general-purpose usages, such as the lodge, medical station, kitchen, and base station. One controls the 220 V_{AC} power for emergency lighting. On the other hand, after reorganizing the power lines of the PV arrays, the sixth PV array is back online, where a 16.7% solar capacity is recovered. In addition, it is safe to adjust the power lines of PV arrays at night without affecting the power operation of the lodge.

Installation of cloud EMS. The self-developed cloud EMS [45,46] is installed to remotely monitor the off-grid PV ESS. When there is a problem in the system or the aging of the battery pack begins to worsen, it is convenient for the crew to repair and maintain the system immediately so as to maintain the health of the system and improve the utilization rate of the system. The energy input (from six PV arrays and the diesel generator) and energy output (to the Paiyun Lodge, kitchen, and base station) are monitored (as shown in Figure 12). The total voltages of all energy cabinets are also listed for reference. The cloud server is set up to store energy information in the database for more than 10 years. Its security stability should have the ability to block several basic hacker attacks, e.g., distributed denial of service (DDoS) attacks [73–75]. A backup database server at the local site is also set for data redundancy. Moreover, the EMS can also provide statistical energy data (such as annual total energy generation, annual total energy consumption, etc.) for the competent unit to evaluate the energy usage status.

Many conditions of energy usage can be read from the monitor screen (Figure 12). The current energy input and output are listed in the top row. For example, the current PV power, the power consumption of the lodge, kitchen, and base station, and the diesel generator power are 5.02 kW, 1.08 kW, 158 W, 449 W, and 0 W, respectively. The historical energy input and output data stored in the database can provide detailed energy analysis. For example, within three days, the power variation curve of all PV arrays exhibited a non-smooth curve with many sharp power drops (circle in Figure 12a, reflecting fluctuations in renewable energies [20,21]. The power consumption of the lodge demonstrated a maximum value of 2773 W, a minimum value of 581 W, and a mean value of 1012 W (circle in Figure 12b). The major power peaks of the lodge were contributed by the kitchen (circle in Figure 12c). At the same time, it was verified that high-power appliances (about 1500 W) are used in the kitchen. The power consumption of the base station exhibited a steady value of 455 $\pm$ 14 W with an energy fluctuation of 3.1% (circle in Figure 12d). This fluctuation indicated that no explicit dependence was found. The diesel generator had operated for a while with a peak power of about 6400 W to the ESS (circles in Figure 12e). The differences in the power system before and after its improvement are briefly listed in Table 4.

Transport by alpine workers. Since 2013, transport by alpine workers has been the only way to take cargo up the mountain because of the tragedy of the helicopter crash at Mt. Jade North Peak [76,77]. From Mt. Jade Trailhead at Tataka Saddle (at an altitude of 2610 m (8563 ft)) to Paiyun Lodge (at an altitude of 3402 m (11,161 ft)), the distance is about 8.5 km (5.3 mi), with an altitude rise of 800 m (2625 ft). The handling weight of the alpine worker is generally 30–60 kg. Tools and equipment must be disassembled and packed into packages weighing less than 30 kg for easy handling. This project transports about 300 kg of tools and equipment up the mountain by alpine workers.

Demolition and transportation of old and abandoned facilities. To maintain the natural environment on the high mountain, the old and abandoned facilities should be demolished and transported down the mountain in line with the principles of Leave No Trace (LNT) [78]. This project transports about 300 kg of old and abandoned facilities down the mountain by alpine workers.

Material preparation, occupational safety, quality control, safety and health facilities, etc. (1) Materials for the project are sometimes not readily available. They must be prepared in advance to avoid the inability to carry out construction within the project period due to unforeseen circumstances. (2) Occupational safety is very important during engineering. Engineers must not only have knowledge of safe engineering but also

have relevant protective equipment to protect themselves, such as safety helmets, safety glasses, masks, and electrical insulation equipment. (3) Quality control applies not only to material acquisition but also to construction quality. Appropriate checkpoints can improve construction quality and construction efficiency. One of the ways to improve the quality of construction is to consider the opinions of the supervision unit on carrying out construction. (4) Some local engineering code requirements must also be met. For example, a "construction notification board" and an "occupational safety and health board" should be set up on-site. Engineers require professional licenses to meet local regulations, such as "Safety and health education and training for manager of occupational safety and health affairs."

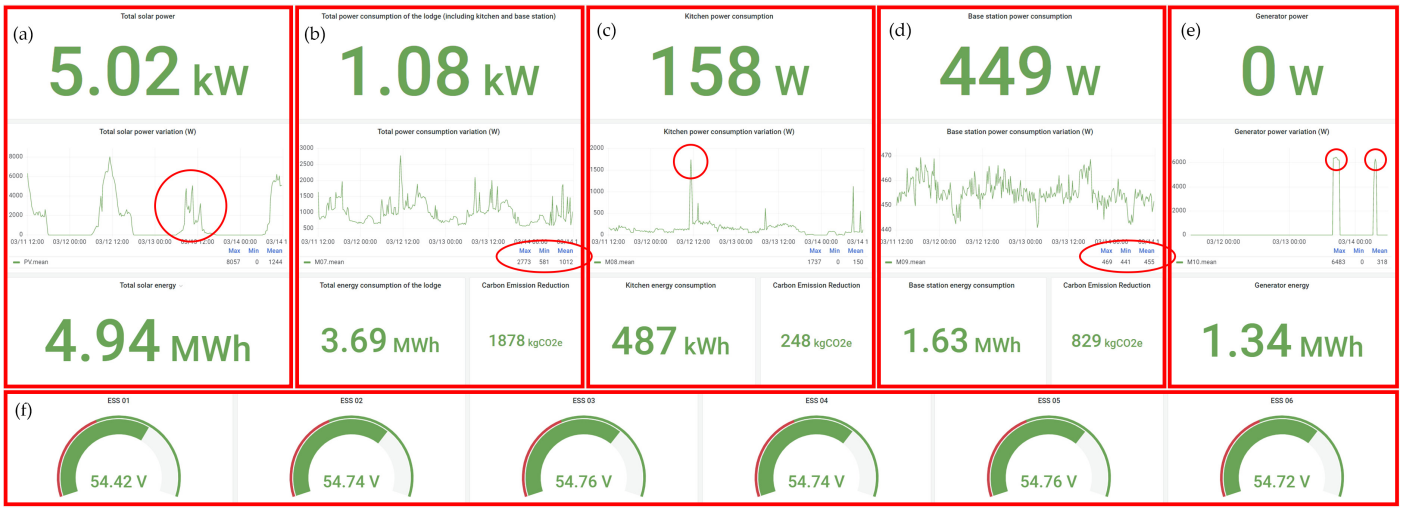


Figure 12. The user monitor screen of the cloud EMS. The screen can be divided into five zones (red rectangles) for analyzing energy information. (**a**) Energy generation information of all PV arrays, including total solar power, total solar power variation, and total solar energy. (**b**–**d**) Energy consumption information of (**b**) Paiyun Lodge, (**c**) the kitchen, and (**d**) the base station, including the total power consumption of the lodge, total power consumption variation (with maximum, minimum, and mean values), total energy consumption, and carbon emission reduction. (**e**) Energy generation information of the diesel generator. (**f**) Total voltages of 6 energy storage cabinets.

Other engineering issues. (1) The establishment of the kitchen power line and the monitoring of its energy usage. During construction, the staff reported that the kitchen may use high-power electrical appliances such as electric cookers, which made the lodge have doubts about the safety of electricity. After all, when the off-grid PV ESS was installed in the past, its energy capacity only accounted for the supply of lighting and medical equipment in the lodge, and the use of high-power electrical appliances in the kitchen was not planned for. Although the total power of the hybrid solar inverters can supply a high-power load, the power lines in the kitchen are pulled from elsewhere using extension cords, which were designed for low-power light-emitting diode (LED) lighting equipment. Under high-power conditions, there may be a public safety problem if the wire is overloaded and melts. In order to solve this problem, after discussion with the chief, an individual power line was pulled from the 110 V_{AC} distribution box for the exclusive use of the kitchen. At the same time, the power monitoring of the individual power line was also carried out. It can be seen from the cloud EMS that high-power appliances are indeed used in the kitchen before the meal period (as shown in Figure 12c). **(2) The insufficient energy capacity of the ESS.** Since the energy consumption of the base station and kitchen was not considered during the design stage of the PV ESS, the energy capacity of the ESS is not sufficient, especially for the aging system. Although, in this project, some new techniques have been applied to extend the life cycle of the system, the lack of energy capacity remains a problem. It is recommended to expand the energy capacity in the future.

Risks and obstacles. Some obstacles to this alpine engineering project are listed. **(1) Acute mountain sickness (AMS).** AMS, caused by rapid exposure to low amounts of oxygen at a place of high altitude, is the most common form of acute altitude illness and typically happens in unacclimatized persons ascending to altitudes > 2500 m (or >8000 ft) [79–83]. People can respond to high altitudes with various symptoms, such as headaches, nausea, vomiting, fatigue, tiredness, confusion, trouble sleeping, and dizziness [84–88]. The incidence of AMS may be accompanied by severe or even fatal high-altitude pulmonary edema (HAPE) [89–95] or high-altitude cerebral edema (HACE) [96–101]. The Lake Louise scoring system (LLSS) was designed to evaluate adults for symptoms of AMS [79,102,103]. Introduced in 1991 and last modified in 2018, it is currently the most commonly used scoring system used to assess AMS [79]. The LLSS uses an assessment questionnaire to determine whether an individual does not have AMS, has mild AMS, or has severe AMS. During climbing or at high altitudes, the LLSS is an appropriate tool to evaluate our health. **(2) The risks of climbing high mountains.** High-altitude climbing has many risks, and engineers (who are also climbers) should be prepared so as to prevent injuries and reduce search-and-rescue events [104,105], e.g., by maintaining adequate physical strength and adequate equipment. **(3) Weather, accidents, and natural hazards.** Low temperatures, strong wind, and rain will make climbing difficult and affect engineering. Typhoons [106–109] and earthquakes [110–114] are common natural disasters in Taiwan. In severe situations, work stoppages or evacuation may be required. During the project period, a severe 6.9-magnitude earthquake occurred on 18 September [115–117], affecting the progress of the project. Including foreshocks, main shocks, and aftershocks, there were about 200 earthquakes in this earthquake sequence [118–121]. When in Paiyun Lodge, we also felt several earthquakes. **(4) The lack of equipment supply.** There are no convenience stores or hardware stores in the high mountains. If we forget to bring tools and equipment, the relevant section can only be abandoned, and the construction can only be carried out after we go up the mountain next time. In particular, for projects on Mt. Jade lasting several days, we must first apply to the Yushan National Park Headquarters. Administrative procedures can also increase time consumption.

The startup operation of the improved power system. The project was completed on 13 October 2022, and the off-grid PV ESS started trial operation (as shown in Figure 13). The completion confirmation meeting was held on 21 October 2022. On 21 November 2022, the project acceptance procedure was carried out, and the system was officially operating.



Figure 13. A site photo after the completion of the off-grid PV ESS improvement (the photo was taken on 10 October 2022). The ESS consisting of six energy storage cabinets is on the left side, and the hybrid solar inverters with major distribution boxes are on the right side. The people standing in the middle are Jung-Feng Jack Lin (**left**) and Hsien-Ching Chung (**right**).

Table 4. Differences in the power system before and after its improvement.

No.	Before Improvement	After Improvement
1	The power system is old and has irregular failures. If a serious failure occurs, the repair time will be long, and the system will be down for a long time. Whether it is an MPPT or a hybrid solar inverter, it has been operating for more than 6 years. Among them, the MPPTs were installed almost two decades ago. These devices are already discontinued products. Repairing them is not an easy task. Even if the manufacturer can provide the products, it might still take several months to half a year to obtain them, which means that the system is shut down for a long time.	Replacing old devices with the new version of hybrid solar inverters can solve the maintenance problem of the system and prevent the system from shutting down for a long time. The over-installation of the hybrid solar inverters is a good strategy for system maintenance and protection on high mountains.
2	The power paths to the ESS are too complex. Having two kinds of power paths increases the probability of failure.	The power path to the ESS has become simple. One kind of power path is used, reducing the failure probability.
3	The power of the 6th PV array cannot be used due to the failure of the 4th MPPT.	Through the new version of the hybrid solar inverter, the power of the 6th PV array can be reconnected to the lodge for use, increasing the energy supply of Paiyun Lodge. About 16.7% solar capacity is recovered.
4	The load is supplied by 3 hybrid solar inverters. The load of each inverter is relatively large, and the service life of the machine will be shorter.	The load is supplied by 6 hybrid solar inverters. The load of each inverter is relatively small, and the service life of the machine will be longer.
5	Since there are only 3 hybrid solar inverters, when one fails, the loads of the other two will increase by 50%, which is relatively dangerous and may lead to the termination of the power supply to the lodge.	Since there are 6 hybrid solar inverters, when one of the inverters fails, the loads of the other five will increase by 20%, which is relatively safe. The system can continue to supply the lodge when one of the inverters fails.
6	The generator transmits power to 3 hybrid solar inverters, and the maximum charging efficiency for the ESS is poor.	The generator transmits power to 6 hybrid solar inverters, and the maximum charging efficiency for the ESS is better.
7	There are 9 distribution boxes full of lines for different systems, resulting in complicated lines and difficult maintenance.	There are 7 distribution boxes, enabling simple wiring and easy maintenance.
8	Some batteries are faulty, causing operation problems in the system.	Fault batteries are replaced by new ones, and the system is restored and works normally.
9	There is an imbalance of battery voltages in the energy storage cabinet.	Active balancers are installed to balance the battery voltages.
10	There is no EMS.	A cloud EMS is installed and can monitor the system remotely. When there is a problem in the system or the aging of the battery pack begins to worsen, it is convenient for the crew to repair and maintain the system immediately so as to maintain the health of the system and improve the utilization rate of the system. At the same time, the EMS can also provide statistical data on energy use, annual total power generation, annual total power consumption, etc., for the competent unit to evaluate the energy use status.

4. Simple Cost Analysis between Medium-Scale Lead–Acid and Li-Ion Battery Systems

Based on the experience of this power improvement project, a brief cost model can be established for the analysis of the usage costs between medium-scale lead–acid and Li-ion battery systems. The total cost (*Cost*) consists of two parts:

$$Cost = Cost_B + Cost_M, \tag{6}$$

where $Cost_B$ is the battery cost, and $Cost_M$ is the extra moving cost due to high mountains.

$$Cost_B = Price_B \times Energy_B, \tag{7}$$

$$Cost_M = Price_M \times (2 \times Energy_B / D_E), \tag{8}$$

where $Price_B$ is the battery price per kilogram, $Energy_B$ is the total energy of the battery system in units of kWh, $Price_M$ is the moving price per kilogram, D_E is the energy density

of the battery system in units of kWh/kg, and "2" indicates uphill and downhill. Before calculation, some assumptions should be noted. Assumption 1: The hybrid inverter can normally work with lead–acid and Li-ion batteries, avoiding cost differences among various inverter systems. Current inverters can use various types of batteries by modifying battery settings. Assumption 2: The labor costs of building the battery systems are very close and can be neglected. Assumption 3: The battery system maintenance costs are very close and can be neglected. Here, the current cost information is listed below. The price of Li-ion batteries per kWh ranges from USD 500 to 2000, with an energy density (D_E) of about 1/16 kWh/kg. The price of lead–acid batteries per kWh ranges from USD 150 to 500, with an energy density of about 1/35 kWh/kg. The extra moving cost from the Tataka Saddle (Mt. Jade entrance) to Paiyun Lodge is about 10 USD/kg.

Taking a battery system with total energy $Energy_B = 100$ kWh as an example, the high and low costs of lead–acid and Li-ion battery systems are shown in Figure 14a. For a Li-ion battery system with a service life of more than 10 years, the high and low costs are the red and blue horizontal dashed lines at USD 232,000 and USD 82,000, respectively. For a lead–acid battery system with a service life of about 2 years, the high and low costs are the red and blue ladder curves, respectively. In the first two years, the lead–acid battery is a good choice. A crossover occurs in the second two-year period (3–4 years), and the Li-ion battery becomes a good choice as of the third two-year period (5–6 years). It is obvious that for the long-term usage of the battery system in the high mountains (or a region where the extra moving cost is very high), the Li-ion battery system is a more economical and environmentally friendly choice. On the other hand, when in a region where there is no extra moving cost, the lead–acid battery will be the cheaper choice for a long time, and the crossover might happen after 8 years, as shown in Figure 14b. This model reasonably explains that general users will choose lead–acid batteries instead of Li-ion batteries, even if they know that lead–acid batteries are highly polluting.

In the above example, the service life is chosen as 2 years based on past battery replacement durations in Paiyun Lodge. Generally, the service life of lead–acid batteries might range from 2 to 10 years, which is highly related to the usage conditions, such as the C-rate and DOD. For a car starter battery, lead–acid batteries are often used at a high C-rate (over $C_R = 3\ \mathrm{h}^{-1}$ for less than 1 second) and very low DOD (less than 1%), and the service life is 2–5 years [122]. For a grid-scale energy storage system, lead–acid batteries are often used at a low C-rate ($C_R < 0.25\ \mathrm{h}^{-1}$) and at a low DOD (less than 50%), and the service life can even be expanded to 10–15 years [123]. However, for lead–acid batteries in Paiyun Lodge, the C-rate was low ($C_R < 0.25\ \mathrm{h}^{-1}$) and the DOD was very high (close to 100%), so the service life was greatly reduced to roughly 2 years.

The lead–acid battery was invented in 1859 by the French physicist Gaston Planté. It is still one of the most widely utilized battery systems worldwide [124]. However, excessive charging will cause lead–acid batteries to emit hydrogen, oxygen, and some toxic gases. This process is known as "gassing," and toxic gas emissions will result in air pollution. The sulfuric acid gases can react with exposed metals, leading to corrosion problems. Also, lead (Pb) pollution and exposure cause environmental and health problems related to heavy metals. Some lead compounds are extremely toxic. Long-term exposure to even tiny amounts of lead compounds can result in brain and kidney damage, hearing issues, and learning problems in children [125]. Poorly managed tailing and gangue disposal processes can lead to water, soil, and transport pollution problems [126]. On the other hand, Li-ion batteries produce no gassing phenomena during normal operation, meaning no on-site toxic air pollution, corrosion, or heavy metal problems. Hence, Li-ion batteries have become eco-friendly replacements for lead–acid batteries.

More than a decade ago, Li-ion batteries were costly to produce. Li-ion battery packs cost 1183 USD/kWh in 2010 [127]. Nine years later, in 2019, the price had decreased nearly tenfold to 156 USD/kWh, falling 87% in real terms [127]. The cost reductions in 2019 resulted from increasing order size, growth in EV sales, and the continued penetration of high-energy-density cathodes. The advance in pack designs and falling manufacturing

costs will drive prices down. The prices for Li-ion battery packs across all sectors reached USD 151/kWh in 2022 [128]. BloombergNEF predicts that Li-ion battery costs will fall below USD 100/kWh in 2024 and hit around USD 60/kWh by 2030 [127,128]. The continued low price of Li-ion batteries will make them more likely to replace lead–acid batteries.

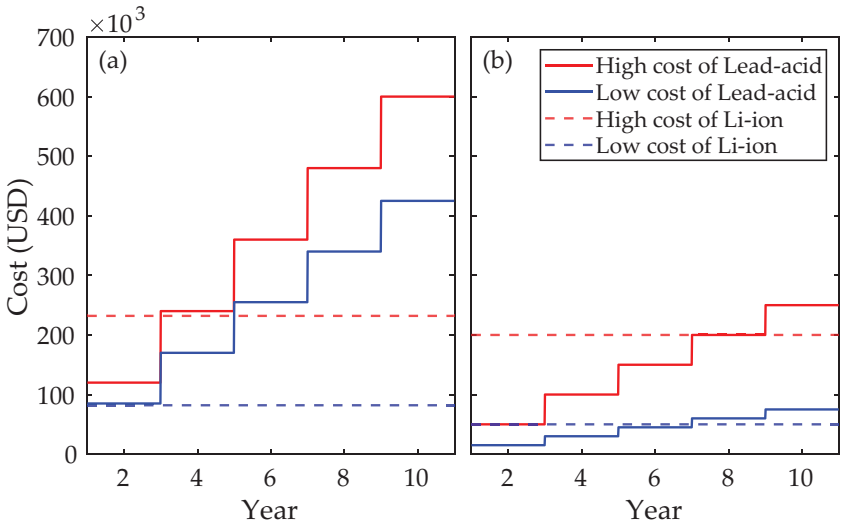


Figure 14. A cost analysis of Li-ion and lead–acid battery systems. (**a**) Cost analysis with the extra moving cost included. The red and blue curves indicate the high and low costs of lead–acid battery systems, respectively. The red and blue dashed lines indicate the high and low costs of Li-ion battery systems, respectively. (**b**) Cost analysis without the extra moving cost.

5. Conclusions

In the context of Li-ion battery analysis, a data processing method has been developed for dealing with large-scale datasets. Four major daily operation patterns are classified based on the conditions of solar and backup energy. The low-C-rate distribution ($C_R < 0.15\ \mathrm{h}^{-1}$) prevented excessive voltage differences among battery cells in the battery system and prevented heat accumulation on the current collectors, improving system stability and expanding the life of the battery system. The temperature is distributed within the recommended range of operating temperatures (15–35 °C) for more than half of the time, meaning that temperature variations are in the normal region and will not affect the system too much. Also, the temperature difference ΔT is almost always under 5 °C over the whole period analyzed, indicating that the battery system has good temperature uniformity. Overall, the operating temperature and C-rate are close to the minima on the Arrhenius plot, indicating a slower aging rate and a longer life of the battery system. The accumulated capacity (energy) is an important quantity for judging the health of batteries. Compared to the data of LFP batteries with a cycle life of about 2000–4000 cycles, the battery system is far from EOL, with an estimated remaining capacity of more than 95%. The Li-ion batteries installed in Paiyun Lodge remain healthy and can continue to be used.

The electric power improvement of Paiyun Lodge has been accomplished, providing a more durable power system, a more stable battery system, and a more comprehensive EMS. For the Li-ion battery system, faulty battery cells have been replaced, and active balancers for shrinking the voltage differences of battery cells are installed. For the power system, the over-installation of hybrid solar inverters is applied for system maintenance on high mountains. Six hybrid solar inverters are installed, so when one is down, the remaining five can still work with a load increase of 20%. The power of the sixth PV array is reconnected, and about 16.7% solar capacity is recovered. For the EMS, a self-developed cloud EMS has been installed, enabling the remote monitoring of all energy input and output of the off-grid PV ESS. On the other hand, engineering issues on high mountains are given, including (1) transport by alpine workers, (2) the demolition and transportation of old

and abandoned facilities, (3) material preparation, occupational safety, quality control, and safety and health facilities, (4) risks and obstacles. We believe that with the completion of the power improvement project, the re-optimized off-grid PV ESS can provide green electricity to Paiyun Lodge and continue to serve climbers. Above all, this study gives engineers and researchers a fundamental understanding of a real case of the long-term usage of off-grid PV ESSs and engineering on high mountains.

The simple cost model demonstrates that Li-ion batteries (instead of lead–acid batteries) are a better choice for long-term applications on high mountains. Owing to the extra moving cost, the crossover of the cost curves of the two battery systems occurs in the second two-year period (3–4 years), and the Li-ion battery becomes a good choice as of the third two-year period (5–6 years). On the other hand, the continued low price of Li-ion batteries on the market will allow lead–acid batteries to be replaced more quickly in the future.

The EMS will play an important role in future research. The old power system possessed no EMS, meaning no energy data were obtained. This makes it hard to effectively solve energy usage problems. With the installation of an EMS in the new power system, we can gather the energy input and output data of the entire power system, evaluating the entire energy input and output accordingly. PV- and diesel-generated energies, energy consumption, and the charge and discharge energies of the battery system can be evaluated accurately. The durability of over-installed hybrid inverters and the effect of balancers on the long-term usage of the battery system can also be confirmed. As the annual energy data are obtained, we can realize whether the capacities of PV and ESS are sufficiently large or not. If the PV and ESS capacities are not sufficient, we will expand the capacities accordingly. Our goal is to largely reduce GHG emissions by using renewable energies.

Funding: This work was supported in part by Yushan National Park Headquarters, Taiwan, under contract number 111-d08. This work was supported in part by Super Double Power Technology Co., Ltd., Taiwan, under the project "Development of Cloud-native Energy Management Systems for Medium-scale Energy Storage Systems (https://osf.io/7fr9z/, accessed on 4 June 2024)" (Grant number: SDP-RD-PROJ-001-2020).

Data Availability Statement: The data are not publicly available due to privacy constraints.

Acknowledgments: The author (H.-C. Chung) would like to thank the contributors to this article for their valuable discussions and recommendations: Jung-Feng Jack Lin, Hsiao-Wen Yang, Yen-Kai Lo, and An-De Andrew Chung. The author (H.-C. Chung) thanks Pei-Ju Chien for English discussions and corrections, as well as Ming-Hui Chung, Su-Ming Chen, Lien-Kuei Chien, and Mi-Lee Kao for financial support.

Conflicts of Interest: Author Hsien-Ching Chung was employed by the company Super Double Power Technology Co., Ltd. The author declares no conflicts of interest. The funders had no role in the design of the study; in the collection, analyses, or interpretation of data; in the writing of the manuscript, or in the decision to publish the results.

Nomenclature

The following symbols and abbreviations are used in this manuscript:

Symbols

C_{acc}	Accumulated capacity
Cap_N	Nominal ampere-hour capacity
C_{day}	Daily accumulated capacity
C_{day}^{chg}	Daily accumulated charge capacity
C_{day}^{dis}	Daily accumulated discharge capacity
C_{year}^{chg}	Annual accumulated charge capacity
C_{year}^{dis}	Annual accumulated discharge capacity
C_{nom}	Nominal capacity
$Cost$	Total cost of battery system

$Cost_B$	Battery cost
$Cost_M$	Moving cost due to high mountains
C_R	C-rate
CR_{year}^{loss}	Annual capacity loss rates
D_E	Energy density of battery system
ΔC_{day}	Difference between daily accumulated charge and discharge capacities
ΔE_{day}	Difference between daily accumulated charge and discharge energies
ΔT	Difference between maximum and minimum battery cell temperatures
Δt_n	nth interval
ΔV_{avg}	Average voltage difference
E_{acc}	Accumulated energy
E_{day}	Daily accumulated energy
E_{day}^{chg}	Daily accumulated charge energy
E_{day}^{dis}	Daily accumulated discharge energy
E_{year}^{chg}	Annual accumulated charge energy
E_{year}^{dis}	Annual accumulated discharge energy
$Energy_B$	Total energy of battery system
ER_{year}^{loss}	Annual energy loss rates
I	Current
$I(t_n)$	Current value of t_n point
$Price_B$	Battery price per kWh
$Price_M$	Moving price per kg
V	Voltage
V_{cell}	Voltage of battery cell
V_n	Voltage of the nth battery cell
$V(t_n)$	Voltage value of t_n point
V_{tot}	Total voltage
T	Temperature
T_{max}	Maximum temperature of battery cells in pack
T_{min}	Minimum temperature of battery cells in pack
T_n	Temperature detected from nth sensor
t_n	Point in partition of $[a, b]$
°C	Degree Celsius
Abbreviations	
1P2W	One-phase two-wire
3C	Computing, communication, and consumer
3D	Three-dimensional
AC	Alternative current
AMS	Acute mountain sickness
BCE	Before the Common Era
BESS	Battery energy storage system
BMS	Battery management system
CC	Constant current
CC-CV	Constant current-constant voltage
CSV	Comma-separated values
DC	Direct current
DDoS	Distributed denial of service
DOD	Depth of discharge
ECM	Equivalent circuit model
EMS	Energy management system
EOL	End of life
ESS	Energy storage system
EV	Electric vehicle
FCAS	Frequency control ancillary services
GHG	Greenhouse gas
HACE	High-altitude cerebral edema
HAPE	High-altitude pulmonary edema

IEA	International Energy Agency
LED	Light-emitting diode
LFP battery	Lithium iron phosphate battery
Li-ion battery	Lithium-ion battery
LLSS	Lake Louise scoring system
LNT	Leave No Trace
MATLAB	Matrix laboratory
MPPT	Maximum power point tracker
PV	Photovoltaic
SEI	Solid electrolyte interface
USD	United States dollar

References

1. Scrosati, B.; Garche, J. Lithium batteries: Status, prospects and future. *J. Power Sources* **2010**, *195*, 2419–2430. [CrossRef]
2. Armand, M.; Tarascon, J.M. Building better batteries. *Nature* **2008**, *451*, 652–657. [CrossRef] [PubMed]
3. Tarascon, J.M.; Armand, M. Issues and challenges facing rechargeable lithium batteries. *Nature* **2001**, *414*, 359–367. [CrossRef] [PubMed]
4. IEA. *Global EV Outlook 2023*; Report; IEA: Paris, France, 2023.
5. Bassyouni, Z.; Allagui, A.; Abou Ziki, J.D. Microsized Electrochemical Energy Storage Devices and Their Fabrication Techniques For Portable Applications. *Adv. Mater. Technol.* **2023**, *8*, 2200459. [CrossRef]
6. Lodico, J.J.; Mecklenburg, M.; Chan, H.L.; Chen, Y.Y.; Ling, X.Y.; Regan, B.C. Operando spectral imaging of the lithium ion battery's solid-electrolyte interphase. *Sci. Adv.* **2023**, *9*, eadg5135. [CrossRef] [PubMed]
7. Collath, N.; Winner, H.; Frank, A.; Durdel, A.; Jossen, A. Suitability of late-life lithium-ion cells for battery energy storage systems. *J. Energy Storage* **2024**, *87*, 111508. [CrossRef]
8. Goldsmith, V. Introduction to grid-scale battery energy storage system concepts and fire hazards. *Process Saf. Prog.* **2024**, *43*, 357–363. [CrossRef]
9. Trombetta, G.L.; Leonardi, S.G.; Aloisio, D.; Andaloro, L.; Sergi, F. Lithium-ion batteries on board: A review on their integration for enabling the energy transition in shipping industry. *Energies* **2024**, *17*, 1019. [CrossRef]
10. Keck, F.; Lenzen, M.; Vassallo, A.; Li, M.Y. The impact of battery energy storage for renewable energy power grids in Australia. *Energy* **2019**, *173*, 647–657. [CrossRef]
11. Radcliffe, J.C. The water energy nexus in Australia - The outcome of two crises. *Water-Energy Nexus* **2018**, *1*, 66–85. [CrossRef]
12. Ye, Y.D.; Qiao, Y.; Lu, Z.X. Revolution of frequency regulation in the converter-dominated power system. *Renew. Sustain. Energy Rev.* **2019**, *111*, 145–156. [CrossRef]
13. Zeng, H.; Sun, F.; Ge, W.; Su, A.; Gao, K.; Ge, Y.; Li, T.; Zhu, Y.; Shao, B.; Xu, T.; et al. Introduction of Australian 100MW Storage Operation and its Enlightenment to China. In Proceedings of the 2018 China International Conference on Electricity Distribution (CICED), Tianjin, China, 17–19 September 2018; p. 2895. [CrossRef]
14. Fernandez-Munoz, D.; Perez-Diaz, J.I.; Guisandez, I.; Chazarra, M.; Fernandez-Espina, A. Fast frequency control ancillary services: An international review. *Renew. Sustain. Energy Rev.* **2020**, *120*, 109662. [CrossRef]
15. Pagliaro, M. Renewable Energy Systems: Enhanced Resilience, Lower Costs. *Energy Technol.* **2019**, *7*, 1900791. [CrossRef]
16. Aziz, A.; Oo, A.M.T.; Stojcevski, A. Issues and mitigations of wind energy penetrated network: Australian network case study. *J. Mod. Power Syst. Clean Energy* **2018**, *6*, 1141–1157. [CrossRef]
17. Saha, C.K.; Nandi, R.; Akter, S.; Hossain, S.; Kabir, K.B.; Kirtania, K.; Islam, M.T.; Guidugli, L.; Reza, M.T.; Alam, M.M. Technical prospects and challenges of anaerobic co-digestion in Bangladesh: A review. *Renew. Sustain. Energy Rev.* **2024**, *197*, 114412. [CrossRef]
18. Yumbla, J.; Home-Ortiz, J.; Pinto, T.; Catalao, J.P.S.; Mantovani, J.R.S. Optimal operational planning of distribution systems: A neighborhood search-based matheuristic approach. *Sustain. Energy Grids Netw.* **2024**, *38*, 101330. [CrossRef]
19. Basic, B.B.; Krcum, M.; Juric, Z. Propeller optimization in marine power systems: Exploring its contribution and correlation with renewable energy solutions. *J. Mar. Sci. Eng.* **2024**, *12*, 843. [CrossRef]
20. Rahbar, K.; Xu, J.; Zhang, R. Real-Time Energy Storage Management for Renewable Integration in Microgrid: An Off-Line Optimization Approach. *IEEE Trans. Smart Grid* **2015**, *6*, 124–134. [CrossRef]
21. Teleke, S.; Baran, M.E.; Bhattacharya, S.; Huang, A.Q. Rule-Based Control of Battery Energy Storage for Dispatching Intermittent Renewable Sources. *IEEE Trans. Sustain. Energy* **2010**, *1*, 117–124. [CrossRef]
22. Liu, G.N.; Yu, Y.J.; Hou, J.; Xue, W.; Liu, X.H.; Liu, Y.Z.; Wang, W.H.; Alsaedi, A.; Hayat, T.; Liu, Z.T. An ecological risk assessment of heavy metal pollution of the agricultural ecosystem near a lead-acid battery factory. *Ecol. Indic.* **2014**, *47*, 210–218. [CrossRef]
23. Zhu, X.F.; He, X.; Yang, J.K.; Gao, L.X.; Liu, J.W.; Yang, D.N.; Sun, X.J.; Zhang, W.; Wang, Q.; Kumar, R.V. Leaching of spent lead acid battery paste components by sodium citrate and acetic acid. *J. Hazard. Mater.* **2013**, *250*, 387–396. [CrossRef]
24. Chung, H.C. Charge and discharge profiles of repurposed $LiFePO_4$ batteries based on the UL 1974 standard. *Sci. Data* **2021**, *8*, 165. [CrossRef]

25. Chung, H.C.; Nguyen, T.D.H.; Lin, S.Y.; Li, W.B.; Tran, N.T.T.; Thi Han, N.; Liu, H.Y.; Pham, H.D.; Lin, M.F. Electric characteristics evaluation of Li-ion repurposed batteries based on UL 1974. In *First-Principles Calculations for Cathode, Electrolyte and Anode Battery Materials*; IOP Publishing: Bristol, UK, 2021; book Section 15, pp. 15-1–15-8. [CrossRef]
26. Nguyen, T.D.H.; Lin, S.Y.; Chung, H.C.; Tran, N.T.T.; Lin, M.F. *First-Principles Calculations for Cathode, Electrolyte and Anode Battery Materials*; IOP Publishing: Bristol, UK, 2021. [CrossRef]
27. Chung, H.C.; Cheng, Y.C. Summary of Safety Standards for Repurposing Batteries. *Mon. J. Taipower's Eng.* **2020**, *860*, 35. [CrossRef]
28. Chung, H.C.; Cheng, Y.C. Action Planning and Situation Analysis of Repurposing Battery Recovery and Application in China. *J. Taiwan Energy* **2019**, *6*, 425. [CrossRef]
29. Chung, H.C. Failure mode and effects analysis of LFP battery module. *engrXiv* **2018**. [CrossRef]
30. Patel, J.; Patel, R.; Saxena, R.; Nair, A. Thermal analysis of high specific energy NCM-21700 Li-ion battery cell under hybrid battery thermal management system for EV applications. *J. Energy Storage* **2024**, *88*, 111567. [CrossRef]
31. Yagci, M.; Orbeyi, O. Programmable logic controlled lithium-ion battery management system using passive balancing method. *J. Radiat. Res. Appl. Sci.* **2024**, *17*, 100927. [CrossRef]
32. Tekin, M.; Karamangil, M.I. Comparative analysis of equivalent circuit battery models for electric vehicle battery management systems. *J. Energy Storage* **2024**, *86*, 111327. [CrossRef]
33. Waldmann, T.; Wilka, M.; Kasper, M.; Fleischhammer, M.; Wohlfahrt-Mehrens, M. Temperature dependent ageing mechanisms in Lithium-ion batteries—A Post-Mortem study. *J. Power Sources* **2014**, *262*, 129–135. [CrossRef]
34. Jorne, J. C Rating of Batteries: A Misleading Concept C Flux Rather than C Rate. *Electrochem. Soc. Interface* **2018**, *27*, 42–43. [CrossRef]
35. Chen, K.W.; Unsworth, G.; Li, X.G. Measurements of heat generation in prismatic Li-ion batteries. *J. Power Sources* **2014**, *261*, 28–37. [CrossRef]
36. Drake, S.J.; Martin, M.; Wetz, D.A.; Ostanek, J.K.; Miller, S.P.; Heinzel, J.M.; Jain, A. Heat generation rate measurement in a Li-ion cell at large C-rates through temperature and heat flux measurements. *J. Power Sources* **2015**, *285*, 266–273. [CrossRef]
37. Chung, Y.H.; Jhang, W.C.; Chen, W.C.; Wang, Y.W.; Shu, C.M. Thermal hazard assessment for three C rates for a Li-polymer battery by using vent sizing package 2. *J. Therm. Anal. Calorim.* **2017**, *127*, 809–817. [CrossRef]
38. Wu, Y.; Keil, P.; Schuster, S.F.; Jossen, A. Impact of Temperature and Discharge Rate on the Aging of a $LiCoO_2/LiNi_{0.8}Co_{0.15}Al_{0.05}O_2$ Lithium-Ion Pouch Cell. *J. Electrochem. Soc.* **2017**, *164*, A1438–A1445. [CrossRef]
39. Leng, F.; Tan, C.M.; Pecht, M. Effect of Temperature on the Aging rate of Li Ion Battery Operating above Room Temperature. *Sci. Rep.* **2015**, *5*, 12967. [CrossRef] [PubMed]
40. Saxena, S.; Xing, Y.J.; Kwon, D.; Pecht, M. Accelerated degradation model for C-rate loading of lithium-ion batteries. *Int. J. Electr. Power Energy Syst.* **2019**, *107*, 438–445. [CrossRef]
41. Somerville, L.; Bareno, J.; Trask, S.; Jennings, P.; McGordon, A.; Lyness, C.; Bloom, I. The effect of charging rate on the graphite electrode of commercial lithium-ion cells: A post-mortem study. *J. Power Sources* **2016**, *335*, 189–196. [CrossRef]
42. Ma, S.; Jiang, M.D.; Tao, P.; Song, C.Y.; Wu, J.B.; Wang, J.; Deng, T.; Shang, W. Temperature effect and thermal impact in lithium-ion batteries: A review. *Prog. Nat. Sci.-Mater. Int.* **2018**, *28*, 653–666. [CrossRef]
43. Mattinen, U.; Klett, M.; Lindbergh, G.; Lindstrom, R.W. Gas evolution in commercial Li-ion battery cells measured by on-line mass spectrometry - Effects of C-rate and cell voltage. *J. Power Sources* **2020**, *477*, 228968. [CrossRef]
44. Bozorgchenani, M.; Kucinskis, G.; Wohlfahrt-Mehrens, M.; Waldmann, T. Experimental Confirmation of C-Rate Dependent Minima Shifts in Arrhenius Plots of Li-Ion Battery Aging. *J. Electrochem. Soc.* **2022**, *169*. [CrossRef]
45. Chung, H.C.; Nguyen, T.D.H.; Lin, S.Y.; Li, W.B.; Tran, N.T.T.; Thi Han, N.; Liu, H.Y.; Pham, H.D.; Lin, M.F., Engineering integrations, potential applications, and outlooks of Li-ion battery industry. In *First-Principles Calculations for Cathode, Electrolyte and Anode Battery Materials*; IOP Publishing: Bristol, UK, 2021; book Section 16, pp. 16-1–16-43. [CrossRef]
46. Chung, H.C. Engineering integrations, potential applications, and outlooks of Li-ion batteries. *engrXiv* **2020**. [CrossRef]
47. Vayrynen, A.; Salminen, J. Lithium ion battery production. *J. Chem. Thermodyn.* **2012**, *46*, 80–85. [CrossRef]
48. Liu, H.Q.; Wei, Z.B.; He, W.D.; Zhao, J.Y. Thermal issues about Li-ion batteries and recent progress in battery thermal management systems: A review. *Energy Convers. Manag.* **2017**, *150*, 304–330. [CrossRef]
49. Chen, D.F.; Jiang, J.C.; Kim, G.H.; Yang, C.B.; Pesaran, A. Comparison of different cooling methods for lithium ion battery cells. *Appl. Therm. Eng.* **2016**, *94*, 846–854. [CrossRef]
50. Sun, J.; Li, J.G.; Zhou, T.; Yang, K.; Wei, S.P.; Tang, N.; Dang, N.N.; Li, H.; Qiu, X.P.; Chen, L.Q. Toxicity, a serious concern of thermal runaway from commercial Li-ion battery. *Nano Energy* **2016**, *27*, 313–319. [CrossRef]
51. Gungor, S.; Cetkin, E. Enhanced temperature uniformity with minimized pressure drop in electric vehicle battery packs at elevated C-rates. *Heat Transf.* **2022**, *51*, 7540–7561. [CrossRef]
52. Liao, Z.H.; Zhang, S.; Li, K.; Zhang, G.Q.; Habetler, T.G. A survey of methods for monitoring and detecting thermal runaway of lithium-ion batteries. *J. Power Sources* **2019**, *436*, 226879. [CrossRef]
53. Lin, C.J.; Xu, S.C.; Chang, G.F.; Liu, J.L. Experiment and simulation of a $LiFePO_4$ battery pack with a passive thermal management system using composite phase change material and graphite sheets. *J. Power Sources* **2015**, *275*, 742–749. [CrossRef]
54. Mahamud, R.; Park, C. Reciprocating air flow for Li-ion battery thermal management to improve temperature uniformity. *J. Power Sources* **2011**, *196*, 5685–5696. [CrossRef]

55. Pesaran, A.A. Battery thermal models for hybrid vehicle simulations. *J. Power Sources* **2002**, *110*, 377–382. [CrossRef]
56. Laidler, K.J. The development of the Arrhenius equation. *J. Chem. Educ.* **1984**, *61*, 494–498. [CrossRef]
57. Arrhenius, S. Über die Reaktionsgeschwindigkeit bei der Inversion von Rohrzucker durch Säuren. *Z. Phys. Chem.* **1889**, *4*, 226. [CrossRef]
58. Arrhenius, S. Über die Dissociationswärme und den Einfluss der Temperatur auf den Dissociationsgrad der Elektrolyte. *Z. Phys. Chem.* **1889**, *4*, 96. [CrossRef]
59. Zhang, Y.C.; Wang, C.Y. Cycle-Life Characterization of Automotive Lithium-Ion Batteries with $LiNiO_2$ Cathode. *J. Electrochem. Soc.* **2009**, *156*, A527–A535. [CrossRef]
60. Liaw, B.Y.; Roth, E.P.; Jungst, R.G.; Nagasubramanian, G.; Case, H.L.; Doughty, D.H. Correlation of Arrhenius behaviors in power and capacity fades with cell impedance and heat generation in cylindrical lithium-ion cells. *J. Power Sources* **2003**, *119*, 874–886. [CrossRef]
61. Schmidt, J.P.; Chrobak, T.; Ender, M.; Illig, J.; Klotz, D.; Ivers-Tiffee, E. Studies on $LiFePO_4$ as cathode material using impedance spectroscopy. *J. Power Sources* **2011**, *196*, 5342–5348. [CrossRef]
62. Yamada, Y.; Iriyama, Y.; Abe, T.; Ogumi, Z. Kinetics of Lithium Ion Transfer at the Interface between Graphite and Liquid Electrolytes: Effects of Solvent and Surface Film. *Langmuir* **2009**, *25*, 12766–12770. [CrossRef] [PubMed]
63. Ogumi, Z.; Abe, T.; Fukutsuka, T.; Yamate, S.; Iriyama, Y. Lithium-ion transfer at interface between carbonaceous thin film electrode/electrolyte. *J. Power Sources* **2004**, *127*, 72–75. [CrossRef]
64. Abe, T.; Fukuda, H.; Iriyama, Y.; Ogumi, Z. Solvated Li-ion transfer at interface between graphite and electrolyte. *J. Electrochem. Soc.* **2004**, *151*, A1120–A1123. [CrossRef]
65. Broussely, M.; Herreyre, S.; Biensan, P.; Kasztejna, P.; Nechev, K.; Staniewicz, R.J. Aging mechanism in Li ion cells and calendar life predictions. *J. Power Sources* **2001**, *97-98*, 13–21. [CrossRef]
66. Bouchet, R.; Lascaud, S.; Rosso, M. An EIS study of the anode Li/PEO-LiTFSI of a Li polymer battery. *J. Electrochem. Soc.* **2003**, *150*, A1385–A1389. [CrossRef]
67. Ossendrijver, M. Ancient Babylonian astronomers calculated Jupiter's position from the area under a time-velocity graph. *Science* **2016**, *351*, 482–484. [CrossRef] [PubMed]
68. Li, J.F.; Wang, D.F.; Pecht, M. An electrochemical model for high C-rate conditions in lithium-ion batteries. *J. Power Sources* **2019**, *436*, 226885. [CrossRef]
69. Saw, L.H.; Ye, Y.; Tay, A.A.O. Electro-thermal characterization of Lithium Iron Phosphate cell with equivalent circuit modeling. *Energy Convers. Manag.* **2014**, *87*, 367–377. [CrossRef]
70. Dubarry, M.; Liaw, B.Y. Development of a universal modeling tool for rechargeable lithium batteries. *J. Power Sources* **2007**, *174*, 856–860. [CrossRef]
71. Wang, J.; Liu, P.; Hicks-Garner, J.; Sherman, E.; Soukiazian, S.; Verbrugge, M.; Tataria, H.; Musser, J.; Finamore, P. Cycle-life model for graphite-$LiFePO_4$ cells. *J. Power Sources* **2011**, *196*, 3942–3948. [CrossRef]
72. Chen, Y.K.; Lin, H.J.; Wu, M.R.; Hsu, H.W.; Yang, A.L. Design and implementation of solar-powered charging system for lithium-ion battery balancing. *Power Electron.* **2016**, *14*, 24–31.
73. Kolias, C.; Kambourakis, G.; Stavrou, A.; Voas, J. DDoS in the IoT: Mirai and Other Botnets. *Computer* **2017**, *50*, 80–84. [CrossRef]
74. Osanaiye, O.; Choo, K.K.R.; Dlodlo, M. Distributed denial of service (DDoS) resilience in cloud: Review and conceptual cloud DDoS mitigation framework. *J. Netw. Comput. Appl.* **2016**, *67*, 147–165. [CrossRef]
75. Peng, T.; Leckie, C.; Ramamohanarao, K. Survey of network-based defense mechanisms countering the DoS and DDoS problems. *ACM Comput. Surv.* **2007**, *39*, 3. [CrossRef]
76. Three killed in helicopter crash in Yushan. Available online: https://news.ltn.com.tw/news/focus/paper/722637 (accessed on 4 May 2024).
77. Mount Jade North Peak Helicopter Crash. Aviation Safety Council: Overweight is the Main Reason. Available online: https://news.ltn.com.tw/news/society/breakingnews/1144740 (accessed on 4 June 2024).
78. The 7 Principles of Leave No Trace. Available online: https://lnt.org/why/7-principles/ (accessed on 4 June 2024).
79. Roach, R.C.; Hackett, P.H.; Oelz, O.; Bartsch, P.; Luks, A.M.; MacInnis, M.J.; Baillie, J.K.; Lake Louise, A.M.S.S.C. The 2018 Lake Louise Acute Mountain Sickness Score. *High Alt. Med. Biol.* **2018**, *19*, 4–6. [CrossRef] [PubMed]
80. Burtscher, M.; Philadelphy, M.; Gatterer, H.; Burtscher, J.; Faulhaber, M.; Nachbauer, W.; Likar, R. Physiological Responses in Humans Acutely Exposed to High Altitude (3480 m): Minute Ventilation and Oxygenation Are Predictive for the Development of Acute Mountain Sickness. *High Alt. Med. Biol.* **2019**, *20*, 192–197. [CrossRef]
81. Honigman, B.; Theis, M.K.; Koziolmclain, J.; Roach, R.; Yip, R.; Houston, C.; Moore, L.G. Acute mountain sickness in a general tourist population at moderate altitudes. *Ann. Intern. Med.* **1993**, *118*, 587–592. [CrossRef]
82. Hackett, P.H.; Rennie, D.; Levine, H.D. The incidence, importance, and prophylaxis of acute mountain sickness. *Lancet* **1976**, *2*, 1149–1155. [CrossRef] [PubMed]
83. Singh, I.; Khanna, P.K.; Srivastava, M.C.; Lal, M.; Roy, S.B.; Subramanyam, C.S. Acute Mountain Sickness. *N. Engl. J. Med.* **1969**, *280*, 175–184. [CrossRef] [PubMed]
84. Horiuchi, M.; Uno, T.; Endo, J.; Handa, Y.; Hasegawa, T. Impact of Sleeping Altitude on Symptoms of Acute Mountain Sickness on Mt. Fuji. *High Alt. Med. Biol.* **2018**, *19*, 193–200. [CrossRef] [PubMed]

85. Cheng, F.Y.; Jeng, M.J.; Lin, Y.C.; Wang, S.H.; Wu, S.H.; Li, W.C.; Huang, K.F.; Chiu, T.F. Incidence and severity of acute mountain sickness and associated symptoms in children trekking on Xue Mountain, Taiwan. *PLoS ONE* **2017**, *12*, e0183207. [CrossRef]
86. Issa, A.N.; Herman, N.M.; Wentz, R.J.; Taylor, B.J.; Summerfield, D.C.; Johnson, B.D. Association of Cognitive Performance with Time at Altitude, Sleep Quality, and Acute Mountain Sickness Symptoms. *Wilderness Environ. Med.* **2016**, *27*, 371–378. [CrossRef] [PubMed]
87. Burtscher, M.; Wille, M.; Menz, V.; Faulhaber, M.; Gatterer, H. Symptom Progression in Acute Mountain Sickness During a 12-Hour Exposure to Normobaric Hypoxia Equivalent to 4500M. *High Alt. Med. Biol.* **2014**, *15*, 446–451. [CrossRef]
88. Hansen, J.E.; Harris, C.W.; Evans, W.O. Influence of Elevation of Origin, Rate of Ascent and a Physical Conditioning Program on Symptoms of Acute Mountain Sickness. *Mil. Med.* **1967**, *132*, 585–592. [CrossRef]
89. Joyce, K.E.; Lucas, S.J.E.; Imray, C.H.E.; Balanos, G.M.; Wright, A.D. Advances in the available non-biological pharmacotherapy prevention and treatment of acute mountain sickness and high altitude cerebral and pulmonary oedema. *Expert Opin. Pharmacother.* **2018**, *19*, 1891–1902. [CrossRef] [PubMed]
90. Swenson, E.R.; Bartsch, P. High-Altitude Pulmonary Edema. *Compr. Physiol.* **2012**, *2*, 2753–2773. [CrossRef] [PubMed]
91. Bartsch, P.; Mairbaurl, H.; Maggiorini, M.; Swenson, E.R. Physiological aspects of high-altitude pulmonary edema. *J. Appl. Physiol.* **2005**, *98*, 1101–1110. [CrossRef] [PubMed]
92. Maggiorini, M.; Melot, C.; Pierre, S.; Pfeiffer, F.; Greve, I.; Sartori, C.; Lepori, M.; Hauser, M.; Scherrer, U.; Naeije, R. High-altitude pulmonary edema is initially caused by an increase in capillary pressure. *Circulation* **2001**, *103*, 2078–2083. [CrossRef] [PubMed]
93. Singh, I.; Kapila, C.C.; Khanna, P.K.; Nanda, R.B.; Rao, B.D.P. High-altitude pulmonary oedema. *Lancet* **1965**, *1*, 229–234. [CrossRef] [PubMed]
94. Hultgren, H.N.; Hellriegel, K.; Houston, C.S.; Spickard, W.B. High altitude pulmonary edema. *Medicine* **1961**, *40*, 289–313. [CrossRef] [PubMed]
95. Houston, C.S. Acute Pulmonary Edema of High Altitude. *N. Engl. J. Med.* **1960**, *263*, 478–480. [CrossRef] [PubMed]
96. Turner, R.E.F.; Gatterer, H.; Falla, M.; Lawley, J.S. High-altitude cerebral edema: Its own entity or end-stage acute mountain sickness? *J. Appl. Physiol.* **2021**, *131*, 313–325. [CrossRef] [PubMed]
97. Hackett, P.H.; Yarnell, P.R.; Weiland, D.A.; Reynard, K.B. Acute and Evolving MRI of High-Altitude Cerebral Edema: Microbleeds, Edema, and Pathophysiology. *Am. J. Neuroradiol.* **2019**, *40*, 464–469. [CrossRef]
98. Bailey, D.M.; Bartsch, P.; Knauth, M.; Baumgartner, R.W. Emerging concepts in acute mountain sickness and high-altitude cerebral edema: From the molecular to the morphological. *Cell. Mol. Life Sci.* **2009**, *66*, 3583–3594. [CrossRef]
99. Hackett, P.H.; Roach, R.C. High altitude cerebral edema. *High Alt. Med. Biol.* **2004**, *5*, 136–146. [CrossRef] [PubMed]
100. Basnyat, B.; Subedi, D.; Sleggs, J.; Lemaster, J.; Bhasyal, G.; Aryal, B.; Subedi, N. Disoriented and ataxic pilgrims: An epidemiological study of acute mountain sickness and high-altitude cerebral edema at a sacred lake at 4300 m in the Nepal Himalayas. *Wilderness Environ. Med.* **2000**, *11*, 89–93. [CrossRef] [PubMed]
101. Hackett, P.H.; Yarnell, P.R.; Hill, R.; Reynard, K. High-altitude cerebral edema evaluated with magnetic resonance imaging - Clinical correlation and pathophysiology. *JAMA-J. Am. Med Assoc.* **1998**, *280*, 1920–1925. [CrossRef] [PubMed]
102. Southard, A.; Niermeyer, S.; Yaron, M. Language used in Lake Louise scoring system underestimates symptoms of acute mountain sickness in 4- to 11-year-old children. *High Alt. Med. Biol.* **2007**, *8*, 124–130. [CrossRef] [PubMed]
103. Savourey, G.; Guinet, A.; Besnard, Y.; Garcia, N.; Hanniquet, A.M.; Bittel, J. Evaluation of the Lake Louise acute mountain sickness scoring system in a hypobaric chamber. *Aviat. Space Environ. Med.* **1995**, *66*, 963–967. [PubMed]
104. Suh, K.S.; Kim, T.; Yi, N.J.; Hong, G. Preparation for high altitude expedition andchanges in cardiopulmonary and biochemical laboratory parameters with ascent to high altitude in transplant patients and live donors. *Clin. Transplant.* **2015**, *29*, 1013–1020. [CrossRef] [PubMed]
105. Mason, R.C.; Suner, S.; Williams, K.A. An Analysis of Hiker Preparedness: A Survey of Hiker Habits in New Hampshire. *Wilderness Environ. Med.* **2013**, *24*, 221–227. [CrossRef] [PubMed]
106. Mei, W.; Xie, S.P. Intensification of landfalling typhoons over the northwest Pacific since the late 1970s. *Nat. Geosci.* **2016**, *9*, 753–757. [CrossRef]
107. Chen, C.S.; Chen, Y.L. The rainfall characteristics of Taiwan. *Mon. Weather Rev.* **2003**, *131*, 1323–1341. [CrossRef]
108. Jian, G.J.; Teng, J.H.; Wang, S.T.; Cheng, M.D.; Cheng, C.P.; Chen, J.H.; Chu, Y.J. An overview of the tropical cyclone database at the Central Weather Bureau of Taiwan. *Terr. Atmos. Ocean. Sci.* **2022**, *33*, 26. [CrossRef]
109. Wu, C.C.; Kuo, Y.H. Typhoons affecting Taiwan: Current understanding and future challenges. *Bull. Am. Meteorol. Soc.* **1999**, *80*, 67–80. [CrossRef]
110. Chen, K.C.; Kim, K.H.; Wang, J.H. Dominant periods and memory effect of the 2021 earthquake swarm in Hualien, Taiwan. *Terr. Atmos. Ocean. Sci.* **2022**, *33*, 33. [CrossRef]
111. Lin, C.W.; Shieh, C.L.; Yuan, B.D.; Shieh, Y.C.; Liu, S.H.; Lee, S.Y. Impact of Chi-Chi earthquake on the occurrence of landslides and debris flows: Example from the Chenyulan River watershed, Nantou, Taiwan. *Eng. Geol.* **2004**, *71*, 49–61. [CrossRef]
112. Dadson, S.J.; Hovius, N.; Chen, H.; Dade, W.B.; Lin, J.C.; Hsu, M.L.; Lin, C.W.; Horng, M.J.; Chen, T.C.; Milliman, J.; et al. Earthquake-triggered increase in sediment delivery from an active mountain belt. *Geology* **2004**, *32*, 733–736. [CrossRef]
113. Wang, W.L.; Wang, T.T.; Su, J.J.; Lin, C.H.; Seng, C.R.; Huang, T.H. Assessment of damage in mountain tunnels due to the Taiwan Chi-Chi Earthquake. *Tunn. Undergr. Space Technol.* **2001**, *16*, 133–150. [CrossRef]

114. Kao, H.; Chen, W.P. The Chi-Chi earthquake sequence: Active, out-of-sequence thrust faulting in Taiwan. *Science* **2000**, *288*, 2346–2349. [CrossRef] [PubMed]
115. Davidson, H. Man Dies as Strong Earthquake Topples Building in Taiwan. Available online: https://www.theguardian.com/world/2022/sep/18/taiwan-earthquake-damage-hualien.
116. Wang, Y.Z.; Hsu, B.S. [Updated] 1 Dead and 146 Injured in the 918 Chishang Strong Earthquake in Taiwan, the Track Bridge Fracture Repair is Estimated to be More than 1 Month. Available online: https://theinitium.com/article/20220918-taiwan-struck-strong-earthquake/ (accessed on 4 June 2024).
117. Chuang, C. Quake Damages About 370 Hualien Homes. Available online: https://news.pts.org.tw/article/602016 (accessed on 4 June 2024).
118. Chen, M.H. 918 Aftershocks Increased! 4 "Unusual" Cases Occurred Yesterday. Central Weather Bureau: Need to Observe 1 or 2 Days. Available online: https://tw.nextapple.com/life/20221011/0183C4F3D193EAE0B44ED78875A6C68E (accessed on 4 June 2024).
119. Chan, S.Y.; Chang, M.C.; Chang, T.C.; Chen, K.H. A 5.0 Earthquake Hit Taitung Yesterday, Causing Severe Damage to Dulan Village near the Epicenter. Available online: https://news.pts.org.tw/article/607350 (accessed on 4 June 2024).
120. 918 Strong Earthquake! Aftershocks Continue! A Graphic Warning Meteorological fan: The Epicenter is Trending North. Available online: https://news.ltn.com.tw/news/life/breakingnews/4062233 (accessed on 4 June 2024).
121. Chuang, M. Hualien Residents Sleeping Outside after Earthquake. Available online: https://news.pts.org.tw/article/600550 (accessed on 4 June 2024).
122. Ruetschi, P. Energy storage and the environment: The role of battery technology. *J. Power Sources* **1993**, *42*, 1–7. [CrossRef]
123. May, G.J.; Davidson, A.; Monahov, B. Lead batteries for utility energy storage: A review. *J. Energy Storage* **2018**, *15*, 145. [CrossRef]
124. Kurzweil, P. Gaston Plante and his invention of the lead-acid battery-The genesis of the first practical rechargeable battery. *J. Power Sources* **2010**, *195*, 4424–4434. [CrossRef]
125. van der Kuijp, T.J.; Huang, L.; Cherry, C.R. Health hazards of China's lead-acid battery industry: A review of its market drivers, production processes, and health impacts. *Environ. Health* **2013**, *12*, 61. [CrossRef]
126. Weiss, M.; Dekker, P.; Moro, A.; Scholz, H.; Patel, M.K. On the electrification of road transportation - A review of the environmental, economic, and social performance of electric two-wheelers. *Transp. Res. Part D-Transp. Environ.* **2015**, *41*, 348–366. [CrossRef] [PubMed]
127. BloombergNEF. Battery Pack Prices Fall as Market Ramps uUp with Market Average at $156/kWh In 2019. Available online: https://about.bnef.com/blog/battery-pack-prices-fall-as-market-ramps-up-with-market-average-at-156-kwh-in-2019/ (accessed on 4 June 2024).
128. BloombergNEF. Lithium-Ion Battery Pack Prices Rise for First Time to an Average of $151/kWh. Available online: https://about.bnef.com/blog/lithium-ion-battery-pack-prices-rise-for-first-time-to-an-average-of-151-kwh/ (accessed on 4 June 2024).

Disclaimer/Publisher's Note: The statements, opinions and data contained in all publications are solely those of the individual author(s) and contributor(s) and not of MDPI and/or the editor(s). MDPI and/or the editor(s) disclaim responsibility for any injury to people or property resulting from any ideas, methods, instructions or products referred to in the content.